

Auroral meridian scanning photometer calibration using Jupiter

Brian J. Jackel¹, Craig Unick¹, Fokke Creutzberg², Greg Baker¹, Eric Davis¹, Eric F. Donovan¹, Martin Connors³, Cody Wilson¹, Jarrett Little¹, M. Greffen¹, and Neil McGuffin¹

¹University of Calgary, Alberta, Canada

²Natural Resources Canada Geomagnetism Laboratory

³Athabasca University, Alberta, Canada

Correspondence to: Brian J. Jackel

brian.jackel@ucalgary.ca

Abstract. Observations of astronomical sources ~~provides~~provide information that can significantly enhance the utility of auroral data for scientific studies. ~~Jupiter is used~~This report presents results obtained by using Jupiter for field cross-calibration of 4 multi-spectral auroral meridian scanning photometers during 2011-15 northern hemisphere winters. Seasonal average optical field-of-view and local orientation estimates are obtained with uncertainties of 0.01° and 0.1° respectively. Estimates of absolute ~~photometric~~ sensitivity are repeatable to roughly 5% from one month to the next, while the relative response between different wavelength channels is stable to better than 1%. Astronomical field calibrations and darkroom calibration differences are on the order of 10%. Atmospheric variability is the primary source of uncertainty; this may be reduced with complementary data from co-located instruments ~~such as all-sky imagers~~.

1 Introduction

10 Interactions between the solar wind and the terrestrial magnetic field produce a complex and dynamic geospace environment. Ionospheric phenomena such as the aurora are connected to magnetospheric processes by mass and energy transport along magnetic field lines. Consequently, auroral observations provide information that can be used for remote sensing of distant plasma structure and dynamics. A single ground-based instrument can only view a small part of the global system. ~~Larger scales may be studied with~~, so a combination of instruments at different locations (eg. Figure 1 and Table 1) ~~, but merging~~
15 are required to span larger scales. Merging multiple data sets requires accurate information about device characteristics such as timing, orientation, and absolute spectral sensitivity.

Comprehensive calibration requires specialized equipment and skilled personnel that are typically available only at centrally located research facilities. With sufficient resources it is possible, at least in principle, to determine all device parameters that are required to convert raw instrument data numbers to physically useful quantities. Practical limitations can result in random
20 or systematic uncertainties which may impede quantitative scientific analysis. This is particularly relevant for large networks of nominally identical instruments, where ongoing calibration of each device may be extremely challenging.

Even assuming ideal calibration at a central facility, many auroral instruments must be operated at remote field sites. Transfer between these locations requires a sequence of packing, shipping, and re-assembly that is time-consuming, costly, and may

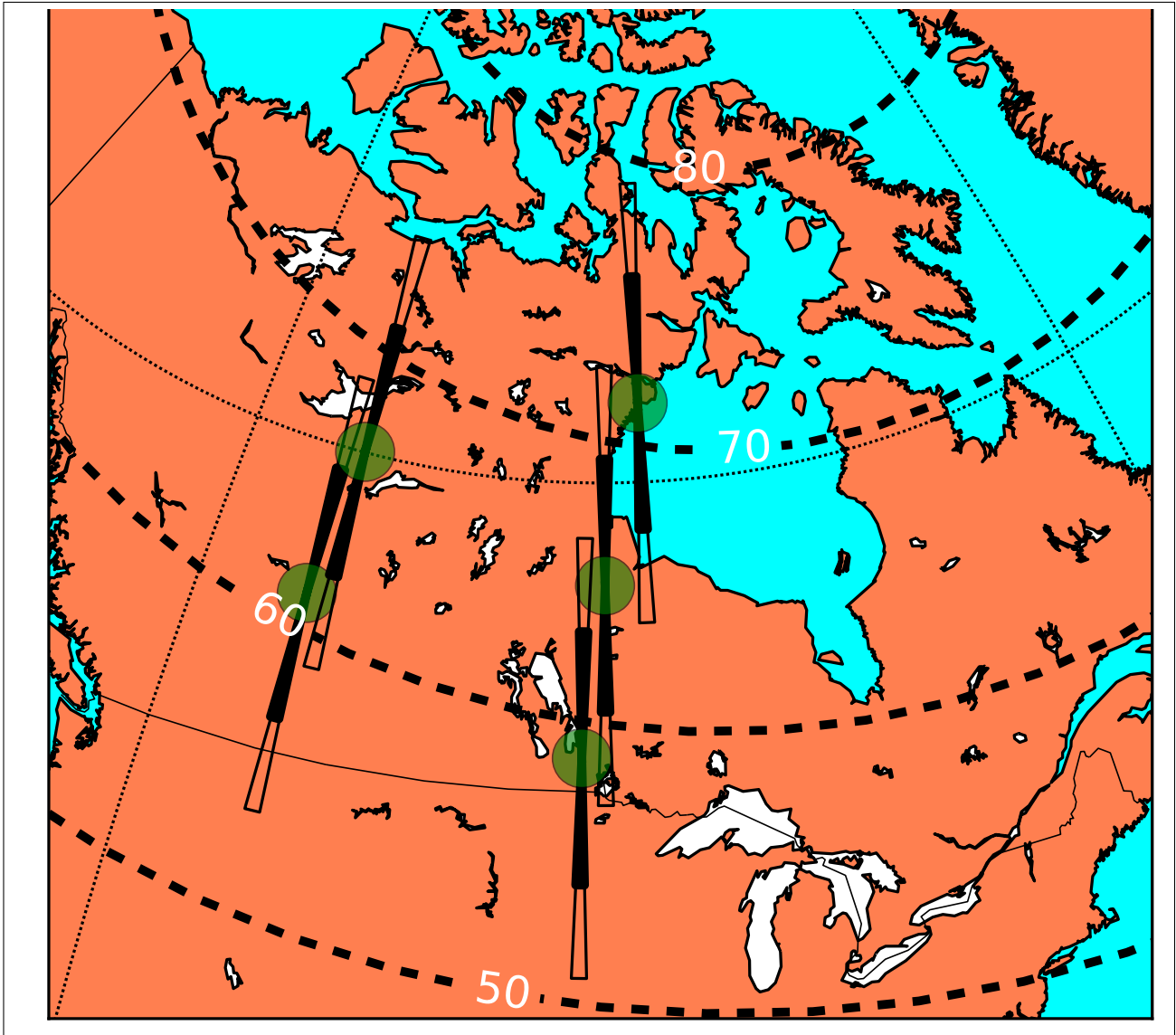


Figure 1. Canadian meridian scanning photometer site locations (details in Table 1). Fan shapes indicate 4° optical beam width for altitudes of 110 and 220 km at elevations of 10° above the horizon. Contours-Dashed contours indicate magnetic dipole latitude (IGRF 20102015).

Table 1. Canadian meridian scanning photometer site information. Geographic latitude, longitude, and altitude are in degrees North, degrees East, and metres above mean sea level (WGS-84). L-shell and magnetic declination **obtained** from the IGRF model.

	Geographic			L-shell		Declination		
	Lat	Lon	Alt	1988	2013	1988	2013	
RANK	62.82	267.89	32	11.20	10.64	-7.1	-7.7	Rankin Inlet, Nunavut
GILL	56.35	265.29	99	6.04	5.83	2.6	-0.5	Gillam, Manitoba
PINA	50.20	263.96	262	3.95	3.84	5.5	2.3	Pinawa, Manitoba
FSMI	60.02	248.05	205	6.65	6.58	24.3	15.8	Fort Smith, NWT
ATHA	54.70	246.70	533	4.50	4.45	21.1	15.3	Athabasca, Alberta

unintentionally alter instrument response. Furthermore, intermittent calibration cannot distinguish between a gradual drift or sudden changes.

Extra-terrestrial sources, such as planets or stars, ~~can be~~ are often used for calibration of spatially resolved optical or radio frequency data. Instrument orientation can be determined from objects whose positions are well known, while source intensity can be used to verify instrument sensitivity. Astronomical sources are often detectable in existing auroral data streams, allowing for ongoing monitoring of system response and the possibility of retrospective re-analysis of older data sets. Practical application may be restricted by instrumental limitations and complications including man-made interference, clouds, aurora and other geophysical processes.

There is a long history of using astronomical sources to determine the alignment of auroral instruments (????). Absolute calibration using stellar spectra appears to be a more recent development (?????). Detailed discussions of these topics are not always provided in the primary scientific literature, but must often be extracted from conference proceedings, technical reports, and theses.

The focus of this paper is on the field calibration of a network of four auroral photometers using Jupiter as a standard reference. Some key features of optical aurorae are provided in Section 1.1, §1.2 introduces key calibration concepts and results, essential astronomical topics are presented in §1.3, and atmospheric effects are briefly reviewed in §1.4. An overview of instrument details is given in §2, data analysis and results are in §3, discussion in §4, followed by a summary and conclusions in §5.

1.1 Optical Aurora

In regions of geospace where magnetic field lines can be traced to the Earth, some charged particles may travel down to altitudes where neutral densities are no longer negligible. Collisions with atmospheric atoms or molecules may transfer energy which can be re-emitted as photons. Spectral, spatial, and temporal features of the optical aurora contain information about geospace plasma properties, allowing for remote sensing of magnetospheric topology and dynamics.

Auroral spectra are dominated by several ~~extremely~~relatively bright lines and bands from atomic oxygen and molecular nitrogen, with many other less intense features ranging from extreme ultra-violet through to far infra-red. The intensity of auroral emission at different wavelengths depends on precipitation energy and atmospheric composition, as more energetic particles are able to penetrate to lower altitudes where constituents may be more or less abundant. Consequently, observations at multiple wavelengths can be combined to infer characteristics of the precipitating particles (??). These multi-spectral measurements can be challenging due to the wide dynamic range between very bright 558 nm “green-line” (1-100 kiloRayleigh) emissions and extremely faint 486 nm “proton aurora” (< 100 Rayleighs).

Optical aurora typically occur within “auroral ovals”, roughly centered around each geomagnetic pole, extending hundreds of kilometres in latitude and thousands of kilometres in longitude (?). Luminosity can be highly dynamic over a wide range of spatial scales, but quiet-time structures generally exhibit a narrow latitudinal extent (10’s to 100’s of km) and relatively less longitudinal variation over 100’s or 1000’s of km (?). This spatial anisotropy is one motivation for using a meridian scanning photometer (MSP, see §2) to measure auroral luminosity as a sequence of latitude profiles (keogram). As shown in Figure 2, this data can also be used to identify other non-auroral features such as clouds and stars.

1.2 Instrument Calibration

Optical designs can be ~~modelled~~modeled very precisely with modern software tools, but instrument calibration provides essential information about the actual performance. System response is not necessarily constant, but can change either gradually (eg. filter bandpass drift, decreased detector sensitivity) or abruptly (eg. damage during shipping). Such problems could be identified with calibration of instruments in the field. This process must be completely automatic, as many remote sites do not have full-time technical staff. It should be repeated frequently in order to identify abrupt changes in system response, but without interrupting or degrading normal data acquisition. A regular schedule of measurements with portable low-brightness sources (LBS) might satisfy some of these requirements, but would involve a substantial allocation of resources for repeated site visits.

In this report we examine some of the strengths and limitations of astronomical calibration for auroral instruments. We focus on issues related to field cross-calibration of MSPs which have been used extensively for auroral research (see §2 for details). However, many of these topics can also be applied more generally to other instruments used to study the optical aurora, such as all-sky imagers (ASIs).

A single ground-based instrument may measure photons with wavelengths λ arriving from angular locations θ, ϕ . ~~External luminosity~~The distribution of incident light I is convolved with the instrument response function f to product a measurement M with error M_ϵ

$$M(\theta, \phi, \lambda) = f(\theta, \phi, \lambda) \star I(\theta', \phi', \lambda') + M_\epsilon(\theta, \phi, \lambda) \quad (1)$$

For an ideal device f would be a delta function and $M = I$, but any real measurement will have limited resolution. The goal of calibration or characterization is to determine the instrument response function f in order to better understand the “true” source properties.

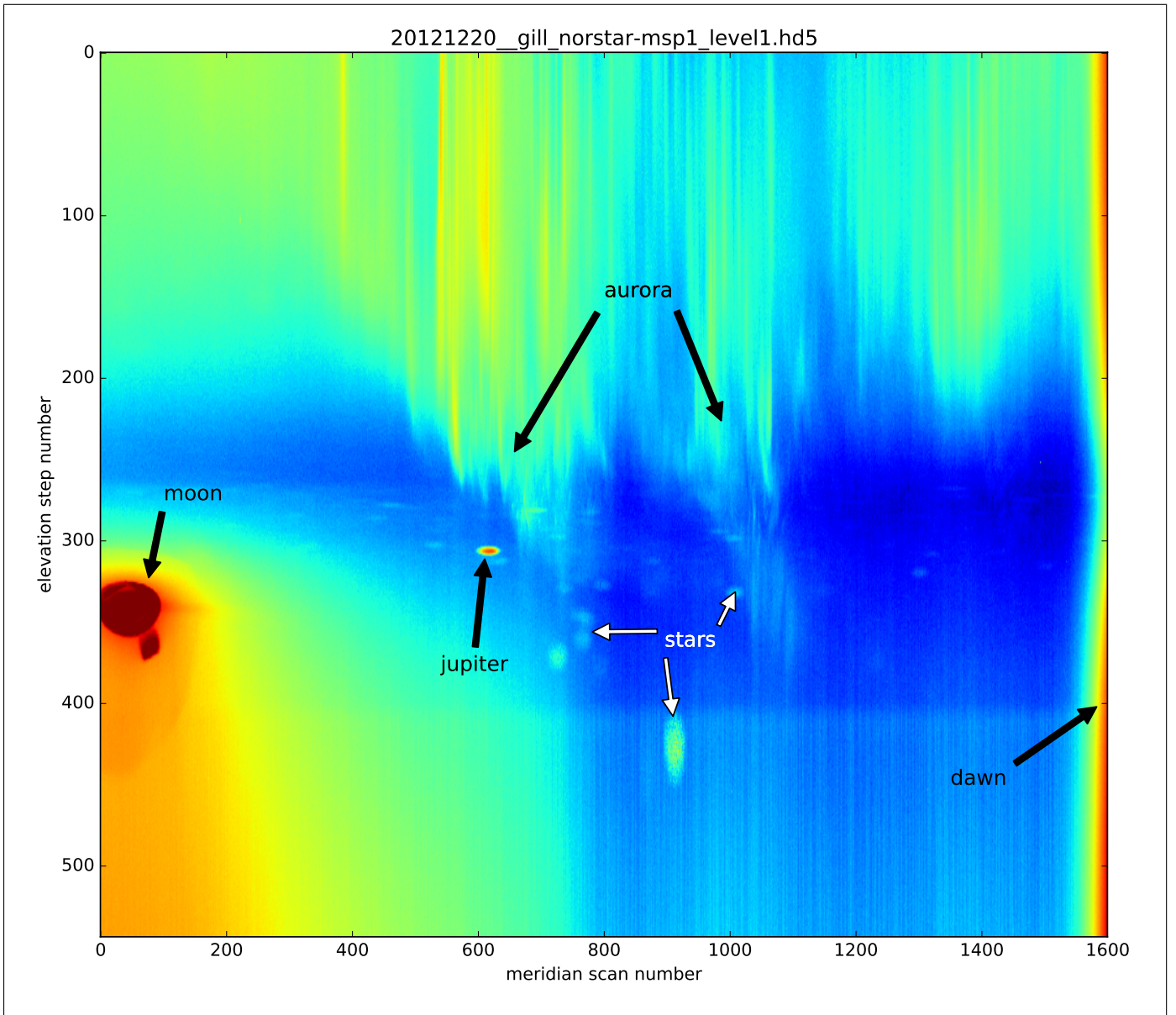


Figure 2. Keogram from meridian scanning photometer operating at Gillam during the night of December 09-2013-20 2012 from 06-0000 UT (local midnight) to dawn at 1320. Local midnight is approximately 0600 (scan number 720). Contrast enhancement was applied to emphasize celestial sources; these are circles. Data counts have been clipped and ellipses most apparent log-scaled in the lower half of the image (zenith order to southern horizon). display Jupiter is the bright feature near scan number 1050, stars, aurora, full moon, and step number 310. dawn.

The general response function in Equation 1 can be separated into a product of geometric sensitivity f_G and spectral sensitivity f_S

$$f_G(\theta, \phi) \times f_S(\lambda) \tag{2}$$

This approximation is not always valid (eg. wide-angle optics coupled to a narrow-band interference filter) but can be usefully applied to many auroral instruments. For convenience we introduce relative response functions (\hat{f}) that are normalized to a maximum of one, and combine all scaling into a single system constant \mathcal{C}

$$\mathcal{C} \times \hat{f}_G(\theta, \phi) \times \hat{f}_S(\lambda) \tag{3}$$

- 5 We show that using Jupiter for field calibration of MSPs provides detailed knowledge about $\hat{f}_G(\theta, \phi)$, estimates of \mathcal{C} that are comparable to darkroom calibration, and useful information about relative spectral response $\hat{f}_S(\lambda)$ at different wavelengths.

1.2.1 Geometric

Calibration for auroral instruments with moderate ($\sim 1^\circ$) angular resolution can be achieved using point-like sources located sufficiently far from the entrance aperture. Angular response can be measured by either moving the source or rotating the
 10 instrument. The effective field-of-view (or “beam shape”) is often azimuthally symmetric around an optical axis with angular polar coordinates θ_0, ϕ_0 , in which case relative response can be expressed in terms of off-axis angle γ

$$\hat{f}_G(\theta, \phi) \approx \tilde{f}_G(\gamma; q_1, \dots, q_N) \tag{4}$$

and some set of instrument parameters q_i (eg. full-width half-max).

Ideally, each instrument would arrive at a field site in exactly the same condition as it left the darkroom. It would be operated
 15 exactly as intended (ie. perfectly level and aligned North/South) without changes for the entire design lifetime. In practice it may be difficult to achieve desired alignment to better than a few degrees. The initial orientation may subsequently drift to some more stable state over months or years, ~~or can change abruptly as new instruments are installed nearby.~~ with the possibility of more abrupt changes as the ground freezes in autumn and thaws in spring. In general, the rotation matrix R required to properly transform from device to local coordinates (eg. azimuth & zenith angle) must be updated regularly in order to ensure that data
 20 are scientifically useful.

Determining Euler angles and geometric response model parameters in the field is relatively straightforward for auroral instruments that can detect and resolve at least a few of the brightest stars. Accurate GNSS site location and measurement timing can be combined with astronomical catalogs to predict the local orientation of each star. These can be converted into device coordinates and used to calculate observable quantities such as transit time and zenith angle. Discrepancies between
 25 predictions and observations can be minimized to determine optimal parameter values. A single night of good data may be sufficient to achieve sub-degree accuracy, which is adequate for many auroral instruments.

Although stars are essentially point sources at infinity, other immutable properties (eg. location, apparent motion, spectral radiance) may make them somewhat less tractable than darkroom calibration sources. Any given object will not always be visible in the night sky or pass through any specific location in an instrumental field of view. However, a substantial amount of
 30 useful information can be gathered over several days or months.

1.2.2 Spectral

The relative spectral response of an instrument is essential for quantitative multi-wavelength analysis, such as estimating precipitation energy (??). Spectral response can be most effectively determined with a monochromatic source

$$\int d\lambda' \hat{f}_s(\lambda') \delta(\lambda - \lambda') = \hat{f}_s(\lambda) \quad (5)$$

- 5 that can scan through the wavelength range of interest. For narrow-band devices it may be sufficient to observe a broad-band source $S(\lambda)$ with known absolute spectral flux density. If the source flux is roughly constant near some wavelength λ_j for each device channel

$$\int d\lambda \hat{f}_s(\lambda) S(\lambda) \approx \bar{S}(\lambda_k) \int d\lambda \hat{f}_s(\lambda) = \bar{S}(\lambda_k) \Delta\lambda_k \quad (6)$$

then the throughput for each channel may be expressed in terms of the effective bandwidth $\Delta\lambda_k$.

- 10 Measurements of an absolutely calibrated low-brightness source (LBS) provide estimates of the differential sensitivity to a continuum source characterized in terms of Rayleighs per nanometer. For discrete emission lines the effective bandwidth is also required in order to determine the sensitivity to brightness as expressed in Rayleighs. The equipment necessary for comprehensive calibration (eg. LBS and monochromator) is not always available at remote field sites, so different methods must be established. Many stellar sources provide spectra which are apparently broad-band at typical auroral instrument resolutions
- 15 on the order of 1 nm. Only relatively bright stars may be above the detection threshold, and absolute flux calibrated spectra are not available for all sources. Still, in certain cases it may be possible for astronomical calibration to produce accurate and repeatable estimates of differential sensitivity.

There does not appear to be a corresponding strategy to determine effective bandwidth in the field. Most stellar spectra are essentially constant in time, so individual sources cannot be used to determine a fixed ~~instrument~~instrument response.

- 20 Combining many different spectra might in principle allow us to distinguish between changes in effective bandwidth and total sensitivity. However, this would require nearly simultaneous observation of multiple absolutely calibrated sources with different spectral types. Low signal levels might also limit the accuracy of any estimates.

For this study we proceed under the assumption that absolute spectral response cannot be independently determined in the field using only astronomical sources. We presume that normalized transmission integrated across each pass-band

$$25 \int d\lambda \hat{T}(\lambda) \equiv \Delta_\lambda \quad \hat{T}(\lambda) = [0, 1] \quad (7)$$

can be obtained in some other way, and acknowledge that simultaneous changes across multiple channels may not be detected using methods considered here. For these reasons, we shall tend to focus on the differential calibration coefficient \hat{C} which can be determined using only astronomical methods. This quantity can also be directly compared to the results of darkroom calibration with an LBS. For auroral studies data numbers \mathcal{D} must be converted to Rayleighs \mathcal{R} , and effective bandwidth is

- 30 required in order to calculate $\mathcal{C}_{\mathcal{R}/\mathcal{D}}$.

1.2.3 ~~Photometry~~Radiometry

~~A-At a distance R from an isotropic point source with total power output (radiant flux) P_0 and isotropic radiant intensity will produce radiance the irradiance (intensity) S which falls off as distance squared. An will be~~

$$S = \frac{P_0}{4\pi R^2} \quad \text{watt} \cdot \text{meter}^{-2} \quad (8)$$

~~so that an~~ observer at some distance r will intercept an amount of power

$$5 \quad P_\delta = S A_{\text{eff}} \quad (9)$$

proportional to the effective receiver surface area A_{eff} .

Power from an extended source can be expressed in terms of a volume emission rate $\rho(r, \theta, \phi)$ integrated over the entire source region weighted by the receiver angular sensitivity $G(\theta, \phi)$

$$P_V = \iint d\Omega \frac{L G}{4\pi} \quad 4\pi L \equiv \int_0^\infty dr \rho(r) \quad (10)$$

10 where the radial integral L has units of radiance ($\text{watt} \cdot \text{meter}^{-2} \cdot \text{sr}^{-1}$) and is often referred to as the ‘‘column emission rate’’. For a uniform source radiance the total received power

$$P_V = \iint d\Omega \frac{L(\theta, \phi)}{4\pi} A_{\text{eff}} \hat{G}(\theta, \phi) \approx L A_{\text{eff}} \Omega_0 \quad (11)$$

depends on the product of the effective area and the effective solid angle. ~~When signals are~~ For any signal detected from some point source ~~, we might ask what there will be an~~ equivalent volume emission which would produce the same observed power.

15 For a uniform emission region the ~~result relationship~~

$$P_\delta = P_V \quad \rightarrow \quad L = \frac{S}{\Omega_0} \quad (12)$$

depends only on the effective solid angle.

Auroral ~~intensities are~~ intensity \mathcal{I} is customarily expressed in units of Rayleighs (????) which is related to photon radiance L_γ via

$$20 \quad 4\pi L_\gamma(\lambda) \equiv \mathcal{I}(\lambda) \quad 10^{10} \text{ photon} \cdot \text{s}^{-1} \cdot \text{m}^{-2} \quad (13)$$

where the subscript E indicates energy flux and γ is photon number flux. For narrow-band channels

$$\mathcal{I}(\lambda) = \int \dot{\mathcal{I}}(\lambda) \approx \dot{\mathcal{I}} \Delta\lambda = 4\pi \frac{\dot{S}_E}{\Omega_0} \frac{\lambda}{hc} \Delta\lambda \quad (14)$$

converting differential radiant spectral density \dot{S} to equivalent Rayleighs per nanometer $\dot{\mathcal{I}}$ requires only the effective solid angle, which can also be estimated from observations of a point source. Working with Rayleighs requires some additional

25 knowledge in the form of the effective bandwidth $\Delta\lambda$. As this is also true for darkroom LBS calibration, we focus here on relating $\dot{\mathcal{I}}$ in Rayleighs per nanometer to \dot{S} in Watts per metre-squared per nanometer.

1.3 Astronomical sources

Extra terrestrial objects have many properties which are required for accurate calibration. Locations in the celestial sphere are known to arc-second resolution or better, which is ~~more than enough to determine the~~ sufficient for determining orientation and geometric response of most auroral instruments. Absolute spectral irradiance profiles are available for many sources, providing 5 opportunities for ~~photometric-radiometric~~ calibration of narrow-band instruments. Total visible intensity of most sources is essentially constant, allowing for long term monitoring of system performance. A single object can be viewed simultaneously by multiple instruments at nearby sites, facilitating quantitative inter-comparisons.

Most astronomical objects are effectively point sources, ~~which is convenient for geometric calibration, but can introduce complications for auroral instruments designed to observe extended emission regions. Only the brightest stars can produce~~ count rates comparable to background contributions such as airglow . and under good viewing conditions modern all-sky imagers can resolve hundreds of stars with a relatively short exposure time. Ironically, the presence of bright aurora or airglow can be a major source of error in radiometric calibration. For the MSP considered here, the total light from Vega passing through through a 3 nm filter is approximately 200 Rayleighs, which is comparable to typical red-line airglow emissions. Even on a moonless night, continuum emissions can be on the order of 10 R/nm, equivalent to stars of magnitude 2 as observed by our MSP. Note that there are only 50 stars of magnitude 2 or brighter, and fewer than half of them are visible from the northern auroral zone at any given time. 10 15

Celestial source brightness spans a wide range and is usually expressed in terms of logarithmic magnitude m

$$I = \sqrt[5]{100}^m \approx 2.512^m \quad (15)$$

so that the relative intensity of two sources can be determined from the difference of their magnitudes. Absolute flux distributions as a function of wavelength are available for most of the brightest stars, including Vega (?), Sirius (?), and Arcturus (??). 20 Other catalogs contain many other stars (????), but the majority may be too dim for reliable observation by typical auroral instruments.

Table 2. Selected astronomical source irradiance at Earth. Energy flux is Joules per $[s \cdot m^2 \cdot nm]$ and number flux is photons per $[s \cdot m^2 \cdot nm]$ Rayleighs are for a viewing solid angle of $\Omega = 0.002$ steradians (2.9° of arc).

	[nm]	[J]	[#]	[R / nm]
jupiter	486	4.78e-10	1.17e+09	735
jupiter	556	5.45e-10	1.53e+09	958
sirius	556	1.35e-10	3.78e+08	237
vega	556	3.44e-11	9.63e+07	60.5
moon	556	4.63e-06	1.3e+13	8.14e+06
sun	556	1.81	5.07e+18	3.18e+12

Conversely, the sun is so bright that direct observation will saturate detectors designed for relatively faint aurora. ? provide an absolutely calibrated distribution of flux versus wavelength at 1 AU with sub-nanometer spectral resolution. For a nominal

instrument solid angle of 2 milli-steradians (3° of arc) the apparent solar brightness at 556 nm is roughly 3 teraRayleighs per nanometer (Table 2). Daytime operations are only possible for systems that respond to an extremely narrow range of wavelengths (?).

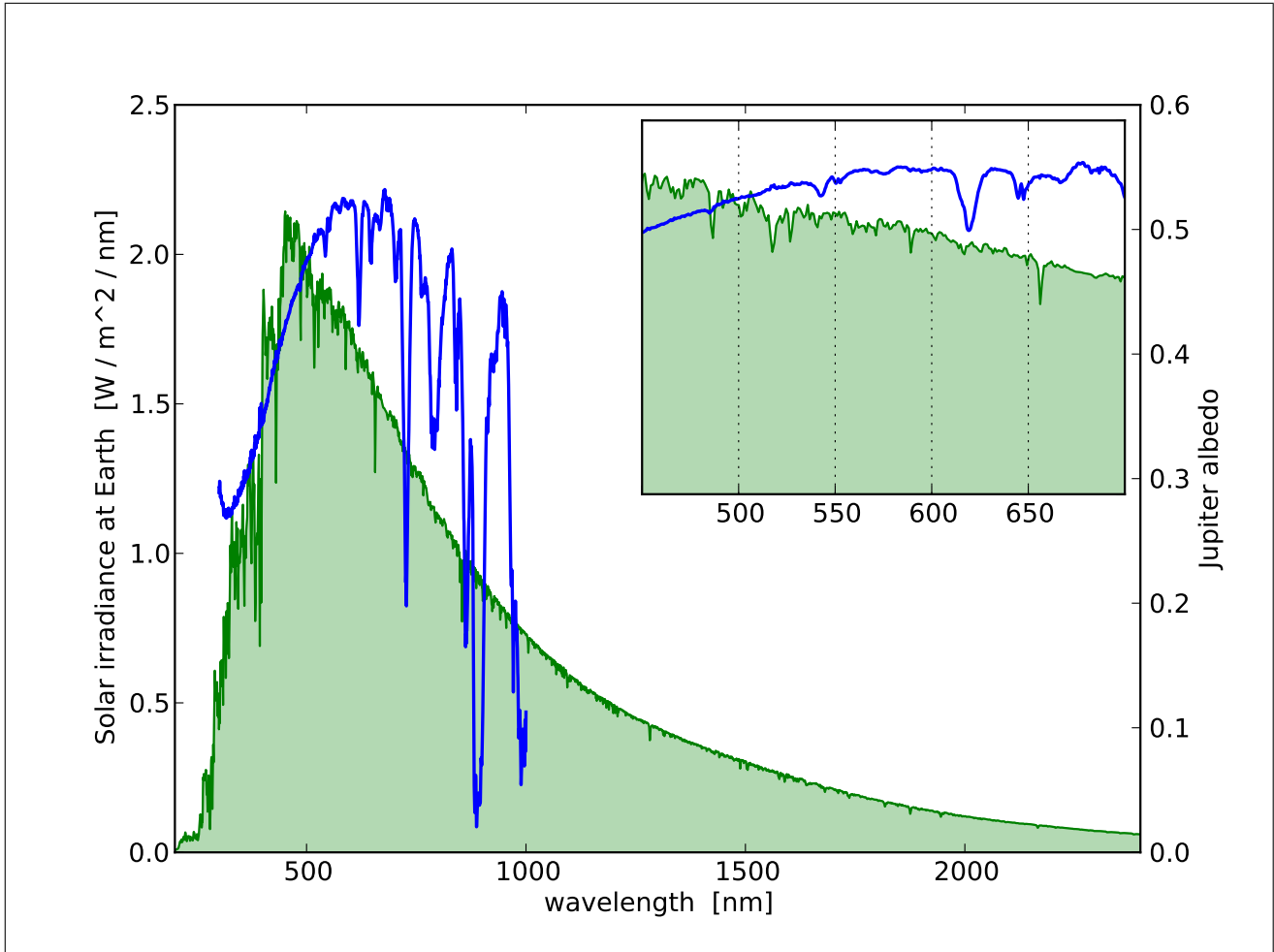


Figure 3. Spectra of solar irradiance (upper-green shaded curve) (?) from ? and Jupiter albedo (?) (blue line) from ?. Inset contains-displays the same quantities in-visible-wavelength-for the range of wavelengths associated with most visible aurora.

Although direct sunlight is unsuitable as a calibration source for most auroral instruments, scattering from other bodies in the solar system can provide more reasonable levels of brightness. The irradiance of an arbitrary body x can be modeled by isotropic emission from the sun incident on a sphere with radius R_x at distance D_{Sx} , followed by scattering and absorption leading to some fraction of flux travelling a distance D_{xE} to arrive at the top of Earth's atmosphere. We can group terms that depend on wavelength and time into $B(\lambda)$ and time and wavelength into $A(t)$ and $B(\lambda)$ respectively

$$I_{xE}(\lambda, t) = A(t) \times B(\lambda) \tag{16}$$

where the solar power $P_s(\lambda)$ and planetary albedo ϵ are both assumed to be time independent to 1% or less. We may express The wavelength dependent term $B(\lambda)$ contains irradiance in terms of the total solar irradiance (TSI ~ 1360 watts/metre-squared) at a fixed distance of 1 AU

$$B(\lambda) \equiv TSI(\lambda) \epsilon(\lambda) \quad (17)$$

5 where the solar power $P_s(\lambda)$ and planetary albedo ϵ are both assumed to be time independent to 1% or less.

~~A phase correction term~~ The time dependent term $A(t)$ contains a phase correction factor $\Phi(\varphi)$ which accounts for any non-Lambertian scattering as a function of angle φ between illumination and observer.

$$A(t) \equiv \frac{R_x^2 D_{SE}^2}{D_{Sx}^2 D_{xE}^2} \Phi(\varphi) \cos(\phi) \quad (18)$$

For example, illumination from a full moon ($\phi = 0$) is reduced by a factor of $3e-6$ ($m \sim 14$) relative to direct sunlight. Despite this substantial decrease, the equivalent brightness of ~~roughly one megaRayleigh~~ nearly 10 megaRayleighs per nanometer (Table 2) is still a hundred times brighter than the brightest aurora. For many instruments the angular size of the moon is neither point-like nor beam-filling, requiring careful attention to details such as wavelength dependent albedo varying across the disk (?), and making phase calculations more complicated. For these reasons, the moon is not commonly used for calibrating auroral instruments.

15 After the moon, Jupiter is currently the brightest celestial object that can be regularly observed well past astronomical twilight. Peak visible magnitude is nearly four times Sirius (the brightest star), making Jupiter easy to identify in the night sky. A detailed spectral distribution of Jupiter's albedo is given by ?. This can be combined with the solar spectrum of ? to predict the wavelength dependence of reflected light given in Table 3.

Other bodies in our solar system are less suitable as calibration sources. Mercury is only visible from Earth during the daytime when looking near the sun. Venus can often be seen near dawn or dusk, but always with excessive amounts of indirect sunlight. Mars can be visible at night for several months in a row, but this ideal configuration only occurs on alternate years. (Figure 5). Albedo can vary considerably during dust storms and a wide range of φ means that the phase function Φ must be very precisely determined (?). Saturn is roughly one-tenth as bright as Jupiter, with complex albedo variations due to ring geometry ($V = -0.62$ to $+1.31$) (?). The remaining outer planets are simply too dim for reliable detection by most auroral instruments.

As Jupiter and Earth each orbit around the Sun, their relative motion produces significant variations in apparent magnitude and position as shown in Figure 4. In recent years Jupiter and the Earth have been closest during winter in northern hemisphere, maximizing brightness during the optimal period for observations with auroral instruments. As shown in Figure 5, Jupiter transit at Gillam Manitoba currently occurs near sunrise in early October and sunset in February. An orbital period of 11.89 years means that opposition will advance by roughly one month per year. Optimal configurations with transit near midnight during northern winter started in 2011, will continue until 2016, and then begin again in 2022. Previous windows of opportunity include 1988-1993 and 1999-2005. Any historical data acquired during these years could conceivably be retrospectively calibrated using Jupiter.

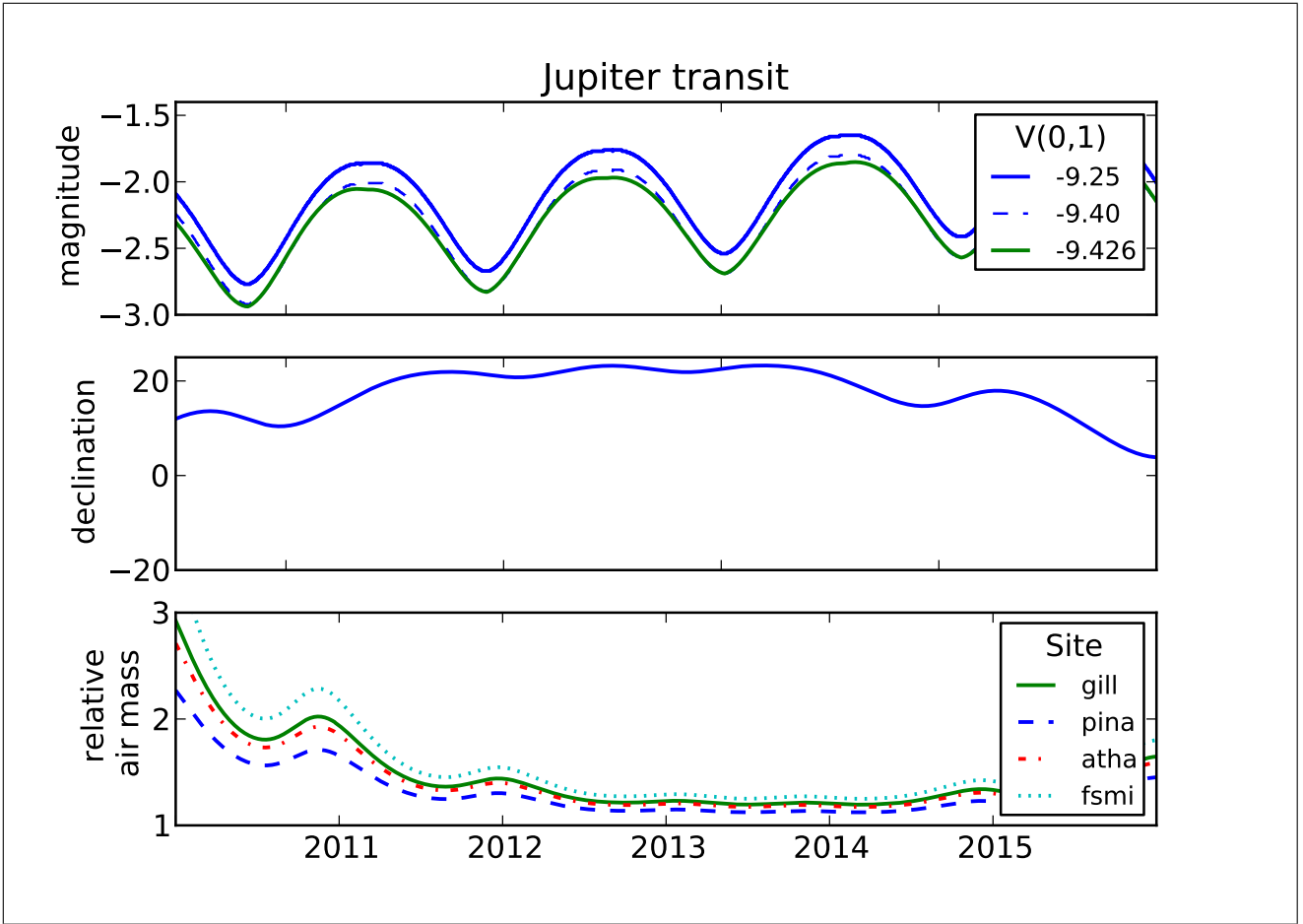


Figure 4. Jupiter as seen from northern auroral zone from 2009 to 2014.¹ Top: apparent visual magnitude (negative is brighter). Different curves correspond to results from older references ($V(1,0) = -9.25$), newer references (-9.40) and calculations in this study (-9.426). Middle: declination, which is effectively the same for any terrestrial observer (parallax ≈ 0). Bottom: relative air mass for during transit at Fort Smith, Gillam, Athabasca, and Pinawa.

During in this study we identified a systematic difference between our flux calculations for Jupiter and the corresponding magnitude value provided by widely available astronomy software (?) using the formula

$$V = V(1,0) + 5 \log_{10}(dr) + \Delta m(i) \quad (19)$$

where $V(1,0)$ is the magnitude at 1 AU with $i = 0$ and $\Delta m(\phi)$ is the magnitude phase correction. Our results were calculated by entering standard distances into Equation ??-18 with irradiance and reflection from ? and ?. We obtained equivalent values of $V(1,0) \approx -9.426$ that were nearly 20% larger than the standard result of $V(1,0) = -9.25$. Eventually we discovered that the widely used lower value came from the 2nd edition of the Explanatory Supplement to the Astronomical Almanac (?) but the most recent 3rd edition (Table 15.8 ?) now indicates $V(1,0) = -9.40$, which differs from our results by only 2%. This

exemplifies the level-at-which-we-were-able-degree-to-which-we-attempted to cross-check our results against other references. It also demonstrates that even astronomical “constants” may be a work in progress.

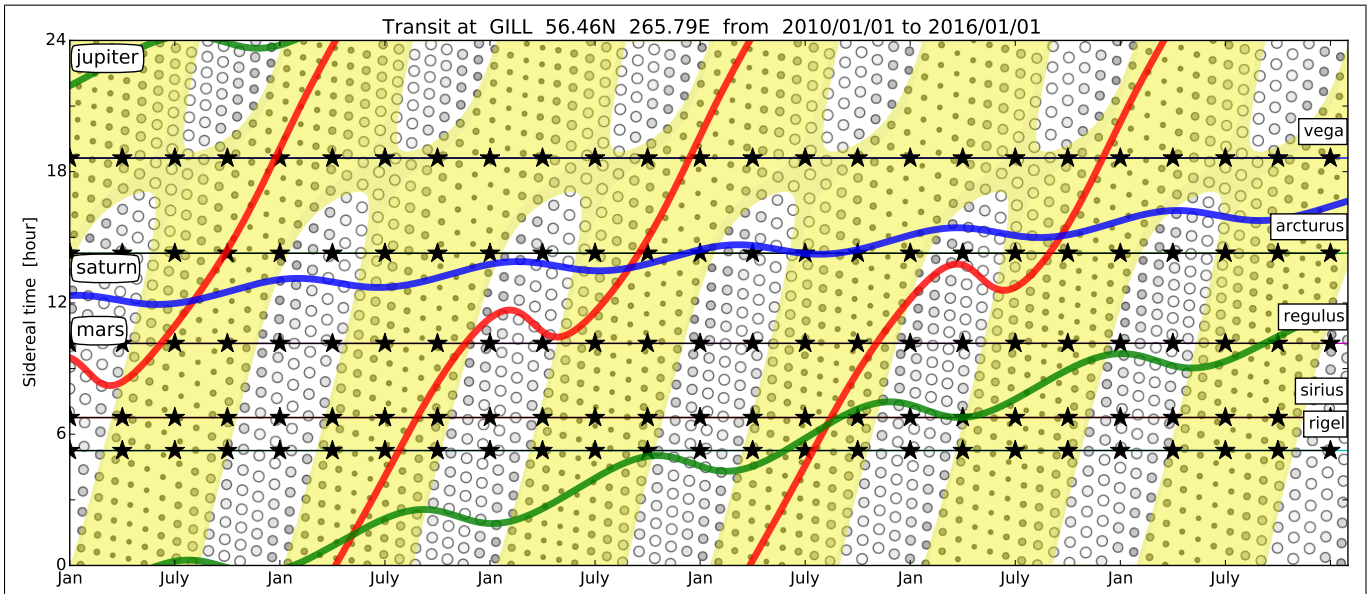


Figure 5. Planetary right ascension over time indicated by thick colored lines (Mars is red, Saturn is blue, and Jupiter is green). Stars indicated by thin black lines remain at constant RA. Yellow contours correspond to daytime between nautical sunrise and sunset (6° below horizon). Size of small circles are proportional to lunar phase with yellow indicating daytime extending to nautical twilight (6° below horizon).

1.4 Atmospheric effects

Light arriving at the top of the Earth’s atmosphere may undergo significant changes by the time it arrives at a ground-based observer. Gradients in the refractive index will bend ray paths, changing the apparent arrival angle. The magnitude of this effect increases with zenith angle but is only on the order of 5 arc-minutes at 10° elevation above the horizon. This might be important for astronomical applications, but is negligible for most optical auroral devices with precision requirements on the order of 1° .

In contrast, variations in atmospheric transmission can be important even at moderate zenith angles. Atmospheric scattering and absorption processes will reduce the radiant flux detected by a ground-based observer (?). The decrease in apparent magnitude can be modelled-modeled as

$$\Delta m(\lambda, \zeta) = \kappa(\lambda) X(\zeta) \quad (20)$$

where $\kappa(\lambda)$ is the extinction coefficient and the relative air mass X as a function of zenith angle ζ

$$X(\zeta) \approx 1 + (1 - c_1)Z - c_2Z^2 - c_3Z^3 \quad Z = \frac{1 - \cos\zeta}{\cos\zeta} \quad (21)$$

is equal to one at the zenith (ie. $X(0) = 1$) and increases by a factor of 5 at 10° elevation above the horizon (?). For convenience we may separate zenith angle and wavelength effects

$$E(\lambda, t) = E_k(\lambda)^{X(t)} \quad E_k \equiv 2.512^{-\kappa(\lambda)} \quad (22)$$

where E_k is the transmission through one standard air-mass (ie. at zenith).

Empirical results from several nights of astronomical observations near sea level (?) show total extinction ranging from $\kappa = 0.312 - 0.604$ and $\kappa = 0.180 - 0.347$ for standard blue and red filters respectively. ? found $\kappa_g = 0.69$ and $\kappa_r = 0.55$ at a low altitude (170m) high humidity location. ? present an extensive review of optical airmass properties for the Arctic and Antarctic.

For this study we use values from ? to provide a lower bound on extinction effects. The upper bound is estimated using an empirical model based on ? and ?.

Table 3. Spectral variation of solar irradiance at Earth (?), albedo of Jupiter (?), and atmospheric extinction at Cerro Paranal (?). Column 5 is the product of solar irradiance at 1AU and Jupiter albedo (defined as $B(\lambda)$ in Equation ??17) with units of watts per metre-squared per nanometre. Atmospheric transmission E_k at zenith is related to extinction κ by Equation 22. Column 8 is the product of solar irradiance, Jupiter albedo, and atmospheric transmission with units of watts per metre-squared per nanometre.

wavelength [nm]	Solar flux [$\text{m}^{-2} \text{nm}^{-1}$]		Jupiter albedo	$B(\lambda)$ [$\text{Wm}^{-2} \text{nm}^{-1}$]	atmosphere		$B(\lambda) E_k(\lambda)$ [$\text{Wm}^{-2} \text{nm}^{-1}$]
	[photon s^{-1}]	[W]			κ	E_k	
470.9	1.783E+018	2.004	0.446	0.893	0.187	0.842	0.752
480.0	1.951E+018	2.096	0.454	0.952	0.179	0.848	0.807
486.1	1.701E+018	1.788	0.455	0.814	0.171	0.854	0.695
495.0	2.027E+018	2.005	0.470	0.942	0.160	0.863	0.813
557.7	2.315E+018	1.799	0.515	0.927	0.127	0.889	0.824
625.0	2.310E+018	1.627	0.495	0.805	0.101	0.912	0.734
630.0	2.481E+018	1.646	0.520	0.855	0.097	0.915	0.782

1.4.1 Transit zenith angle

Zenith angle at transit depends on the observer latitude Λ and declination of the source. Consequently, two observers viewing the same source from different latitudes will be looking through different air masses. This can produce systematic differences in brightness of a few percent or more depending on the latitude offset $\Delta\Lambda$ and extinction E_k

$$I_2/I_1 \propto E_k^{\Delta X} \quad \Delta X \approx \frac{1}{\cos(\zeta_1 + \Delta\Lambda)} - \frac{1}{\cos(\zeta_1)} \quad (23)$$

Calibration using Jupiter (or any other planet) will be further complicated by corrections for varying declination. Figure 4 shows several years variation of air mass for Jupiter transit at the four field sites considered in this study. A significant transition occurs between large latitude dependent extinction before 2011 to relatively uniform low levels afterward. The [effects-consequences](#) for this study are only on the order of a few percent, but are clearly evident in results presented in §3.3.

5 This provides some assurance that our analysis procedures are accurate near the 1% level. Of course, calculating the effects of varying declination requires atmospheric extinction coefficients that may not be very well known. This is a challenge, but also an opportunity to test which extinction models produce the best agreement with observations.

Declination differences can even alter the intensity ratio between two different wavelengths (heterochromatic extinction in ?)

$$10 \quad I_2/I_1 \propto \Delta E_k^{X(\zeta)} \quad \Delta E_k \equiv 2.512^{\kappa(\lambda_1) - \kappa(\lambda_0)} \quad (24)$$

because extinction is a non-linear function of air mass. This effect is considered in §3.4 and found to be significant.

2 Meridian Scanning Photometer

Auroral luminosity is often spatially anisotropic, with latitude structuring on scales of 1-100 km and longitudinal features extending from 100s up to 1000s of kilometres. Consequently, some instruments are designed with reduced azimuthal coverage in exchange for improved sensitivity along a latitude profile. These systems may be referred to as meridian imaging spectrographs (MIS) or meridian scanning photometers (MSP) depending on the technology used for spectral discrimination and photon detection. In this paper we explore issues related to field cross-calibration of a specific MSP design that has been used extensively for auroral research in Canada. Many of these topics can also be applied more generally to other auroral optical devices.

20 Data used for this study were obtained from a network of four multi-spectral auroral meridian scanning photometers. These systems were based on the meridian scanning photometer array (MPA) component of the CANOPUS project (?) which operated MSPs at three sites in a latitude chain: Rankin Inlet, Gillam, Pinawa (the “Churchill line”), and a fourth auroral zone site two hours to the west in Fort Smith. The primary goal was to detect proton aurora at 486.1 nm and electron aurora at several wavelengths (see Table 4) in order to determine precipitation species, characteristic energy, and energy flux. The array was operated continuously for nearly 20 years, producing a large high-quality data set which was the foundation for important research on topics including substorms (?), the polar cap boundary (??), poleward boundary intensifications (??), and the B2i isotropy boundary (?).

30 Due to bandwidth limitations, most raw instrument output was down-sampled by averaging in space and time in order to produce a uniform data stream for real-time transmission. Full high resolution data were available over a serial “campaign port”. In later years, data loggers were used at some sites to record the full resolution data; several years of “high-res” MSP data are available for retrospective re-calibration. The more extensive “low-res” dataset is averaged into 17 latitude bins per scan, which is adequate for auroral science, but diminishes the ability to resolve elevation from individual star transits.

The original CANOPUS MSPs were built by an industrial contractor (?) based on a series of instruments developed at the National Research Council of Canada (NRCC). Calibration of the prototype was carried out in 1985 by NRCC and the University of Saskatchewan; the results of which led to several design modifications. The first field system was commissioned at Gillam in February 1986, with all four units operational by early 1988. By the late 1990's it was increasingly obvious that the instruments were nearing end-of-life. The primary concern was the mirror motors which had driven several billion steps, but many other issues (eg. data acquisition, high voltage supplies, photomultiplier tubes) were also causing problems. Eventually, a lack of spare parts resulted in significant failures and data loss.

An MSP revitalization project was carried out at the University of Calgary starting in 2007. The goal was to provide replacement systems with equivalent functionality. System design was based closely on the original instruments in order to minimize risk, with legacy mechanical and optical components reused where possible. Initial development was carried out on the legacy system at Rankin Inlet which was broken beyond repair. The detector was replaced with a new PMT, high voltage supply, and pulse-counting circuit. Anti-reflection coatings were added to several optical elements, with system throughput optimized with predictions from optical modelling software and confirmed with quantitative testing. All of the old filters were replaced, as was the filterwheel motor. The scanning mirror assembly was upgraded to provide 0.09° elevation steps (4000 steps per 360°). Thermal and power control systems were completely replaced. ~~An FPGA coordinates for low~~ Low level timing and synchronization ~~, while is now coordinated by an FPGA, with~~ a Linux PC-104 ~~was~~ responsible for data acquisition and overall system control.

After darkroom calibration and local field trials the new prototype system was deployed at Gillam and operated adjacent to the legacy system which was still functioning intermittently. The original Gillam system was then upgraded and sent to Fort Smith (2009), the old Fort Smith system upgraded and installed at Pinawa (2010), and the old Pinawa system upgraded and moved to a new site near Athabasca (2011). Additional improvements were implemented in later systems, motivating a round of upgrades in 2012 to the Gillam and Fort Smith units. The entire rebuild process took more than four years and involved multiple personnel at the University of Calgary. Despite careful attention to tracking changes, there are still some functional differences between the first and last refurbished systems. Many of these issues have been identified with internal calibration procedures, but astronomical sources provide useful insight about comparative instrument performance.

The new Calgary MSPs use the same filter-wheel design as CANOPUS to acquire data from eight spectral channels, with 486.1 nm duplicated in order to increase SNR for faint proton aurora. Accurate ~~photometry radiometry~~ of rapidly varying aurora requires effectively simultaneous measurements of background and signal. This is accomplished by rotating the filter-wheel at 1200 RPM (20 Hz) and gating the detector to provide successive 12.5 ms sample spacing. Some details about filter sequencing is given in Table 4; for simplicity all subsequent multi-channel data will ~~presented in wavelength order~~ be ordered by increasing wavelength (blue to red).

Interference filter transmission and blocking as a function of wavelength were provided by the manufacturer and summarized in Table 5. Results were very close to specifications (~~FWHM: FWHM of~~ 3 nm for the blue filters and 2 nm for ~~the others~~) green and red. Transmission peaks were broad and flat with maxima around 80%, which is ~~the key parameter~~ important for optimizing

Table 4. MSP filter wheel sequence.

wavelength [nm]	description	filter wheel position	
		CANOPUS	Calgary
470.9	N_2^+ energy flux	5	6
480.0	blue background (1)	1	2
486.1	H_β (1)	2	3
486.1	H_β (2)	3	4
495.0	blue background (2)	4	5
557.7	OI “green-line”	6	7
625.0	“red-line” background	7	0
630.0	OI “red-line”	0	1

detection of narrow emission lines. The $\Delta\lambda$ effective passband

$$\Delta\lambda_j = \int d\lambda \hat{T}_j(\lambda) \quad (25)$$

is the relevant quantity for broad-band calibration sources ie. converting from Rayleighs per nanometer to Rayleighs. These data suggest typical passband and transmission variations on the order of 5% between different sets of filters.

Table 5. Characteristics of three sets of nominally identical narrow band filters. Passband is integral of transmission profile, 90% bandwidth is the range between 5% and 95% points of the cumulative transmission.

[nm]	passband [nm]			peak transmission [%]			90% bandwidth [nm]		
470.9	2.483	2.362	2.355	82.94	79.36	78.28	3.60	3.40	3.50
480	2.592	2.418	2.661	85.59	78.60	87.74	3.10	3.20	3.20
486.1	2.605	2.587	2.615	88.26	85.95	87.57	2.90	3.00	3.00
486.1	2.572	2.222	2.509	84.71	74.21	83.44	3.10	3.00	3.10
495	2.607	2.525	2.584	88.40	85.74	87.27	3.30	3.40	3.50
557.7	1.788	1.728	1.920	82.93	78.93	88.53	4.60	4.90	4.30
625	1.624	1.632	1.588	84.46	87.37	86.09	4.20	3.20	2.80
630	1.597	1.590	1.558	86.67	84.83	83.81	2.40	2.60	2.40

5 Light which passes through the filters is detected by a photo-multiplier tube (PMT) with photocathode quantum efficiency ranging from 20% at 400 nm to 2% at 750 nm; this response was selected to maximize response for the faint H_β emissions. A dynode chain amplifies each electron to produce a cascade which triggers a pulse-counting circuit. The high-voltage power supply required for this process is quite stable over short intervals under ideal conditions, but may change during extended field operations. Photocathode aging and high-voltage drift are likely to be the primary ~~cause~~ causes of any long-term reduction in

10 system sensitivity.

PMTs dead-time produces a non-linear response at high count-rates. This pulse pile-up effect can be largely removed if the time resolution τ of the system is known and is not significantly longer than the signal count interval. For the PMTs used in this study nonlinearity only becomes important for count rates greater than 10^5 photons per second. These rates can be produced by very bright aurora but are not a problem for any astronomical sources except the Sun and Moon.

5 Meridian scans are achieved with a 45° tilted mirror and a stepping motor. Many MSPs rotate the mirror at a fixed rate in order to produce data from evenly spaced elevations. Both the original and refurbished systems considered here instead utilize a sequence of variable steps chosen to produce nearly constant exposure times as a function of linear distance at auroral altitudes. This detail is relevant to this study because Jupiter transit profiles will be measured with different resolution depending on transit elevation. The effects are expected to be small, but must be kept in mind when considering multi-year variability.

10 2.1 System sensitivity

The relationship between incident photon flux $\mathcal{P}(\lambda)$ and measured channel count rate \mathcal{D}_k

$$\mathcal{D} = A_{\text{eff}} M_x \Delta t \int d\lambda \mathcal{P}(\lambda) T_k(\lambda) Q(\lambda) \quad (26)$$

depends on the effective aperture allowing photons into the system (A_{eff}), channel multiplexing efficiency (M_k), filter transmission (T_k), measurement interval (Δt), and the detector efficiency $Q(\lambda)$.

15 For wide-band input through narrow-band filters the process can be written in terms of filter peak transmission T_k and bandwidth $\Delta\lambda_k$

$$\mathcal{D}(\lambda_i) \approx \mathcal{P}(\lambda_k) A_{\text{eff}} M_k \Delta\lambda_k T(\lambda_k) \Delta t Q(\lambda_i) \quad (27)$$

giving a from which we can isolate a coefficient of response ${}_k\mathcal{C}_{\mathcal{D}/\mathcal{P}}$ for each channel

$$\begin{aligned} {}_k\mathcal{C}_{\mathcal{D}/\mathcal{P}} &= \frac{\mathcal{D}(\lambda_k)}{\mathcal{P}(\lambda_k)} \\ 20 \quad &= A_{\text{eff}} M_x \Delta\lambda_k T(\lambda_k) \Delta t Q(\lambda_k) \end{aligned} \quad (28)$$

in terms of measured \mathcal{D} and predicted \mathcal{P} for each filter wavelength. ~~We will use the term “calibration coefficient” to refer to differential brightness per count which is the quantity of interest when converting data to physical units. However, we will express subsequent results~~ In principle this equation could be used to calculate coefficients in terms of ~~the reciprocal “sensitivity” for which that higher numbers are better~~ fundamental properties of each instrument. In practice, calibration coefficients are
 25 often estimated empirically by measuring sources with known brightness. For auroral applications the goal is to determine the differential sensitivity $\mathcal{C}_{\mathcal{D}/\mathcal{P}}$ relating data numbers to Rayleighs per nanometer.

2.2 Darkroom calibration

All systems have been calibrated at the University of Calgary using a low brightness source (LBS) with spectral radiance measured by the Canadian Institute for National Measurement Standards. Several sets of calibration results for one instrument

at different times are shown in Table 6. Results from two successive days (November 21 & 22 2014) agree to 1% or better, suggesting that the calibration process is highly repeatable. Earlier results from 2010 indicate that the system was about 5% more sensitive in all channels, but with only two measurements over more than 4 years, it is impossible to determine whether this corresponds to a gradual decline or an abrupt change at some time during shipping or field operations.

Table 6. Fort Smith MSP channel sensitivity $C_{\dot{R}/D}$ [Rayleighs/nm/count] determined by darkroom LBS calibration.

Site Date Device	471.0	480.0	486.0	486.0	495.0	557.7	625.0	630.0
fsmi 20100112 msp-02	0.2712	0.2570	0.2446	0.2474	0.2666	4.5029	0.8188	0.8598
fsmi 20141121 msp-02	0.2935	0.2756	0.2647	0.2685	0.2900	5.8267	0.9180	0.9742
fsmi 20141122 msp-02	0.2942	0.2735	0.2645	0.2687	0.2904	5.9789	0.9258	0.9833

5 3 Data analysis

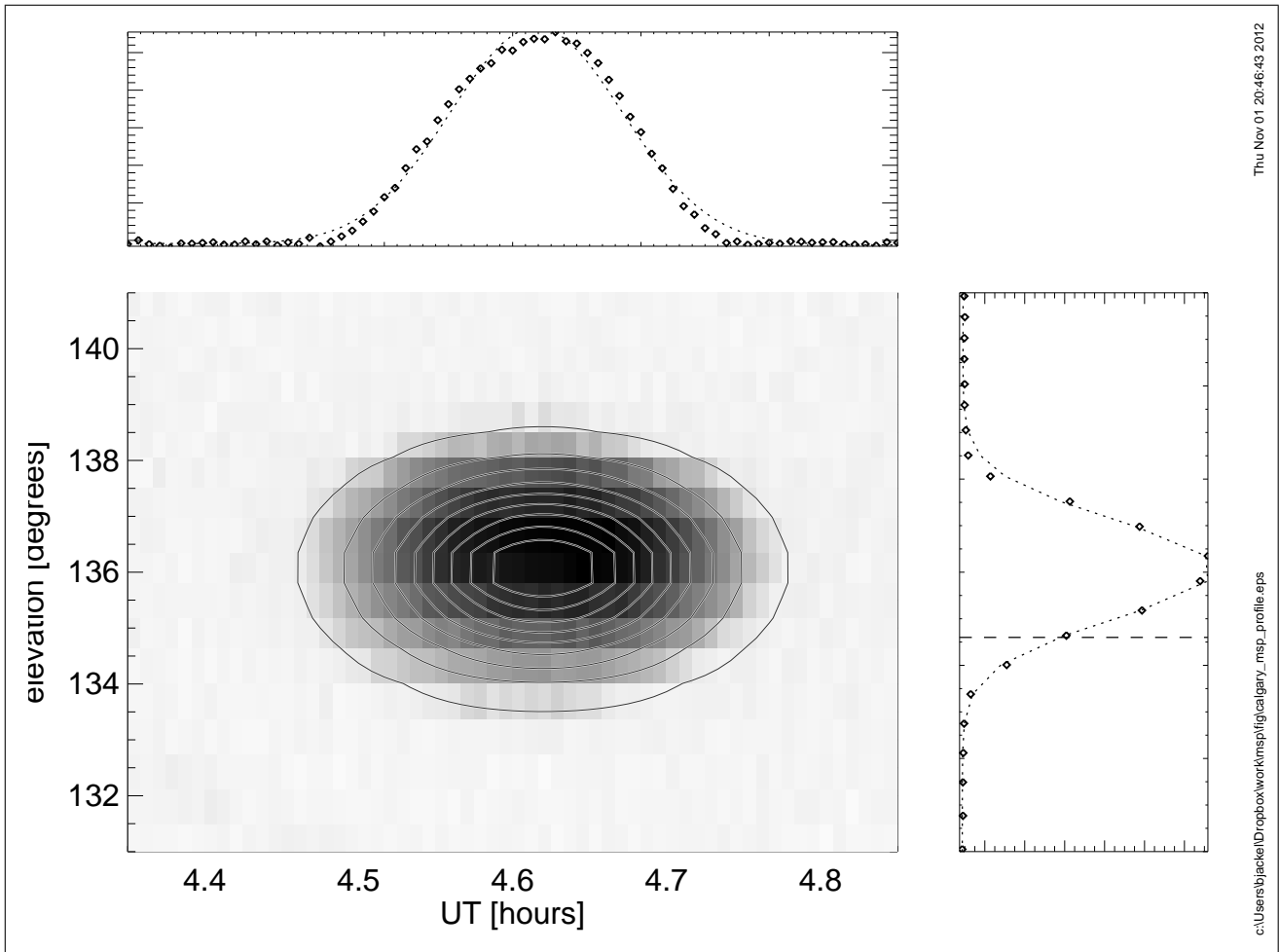
In this section we present methods for extracting useful calibration information from Jupiter transits in MSP data. There are five topics organized by which parameter is under consideration and what supporting measurements are required. ~~with results that~~ Results range from precise and absolute to uncertain and relative. Optical field of view is considered in §3.1, device orientation in §3.2, magnitude variation in §3.3, spectral ratios in §3.4, and absolute sensitivity in §3.5.

10 Each of the MSPs considered in this study ~~executes-repeats~~ a sequence of ~~repeated~~-scans from the northern to southern horizon. Every scan consists of multiple steps through a 160° elevation range, with measurements acquired through multiple filters at each step. The resulting data stream has units of “counts” or simply “data numbers” (D) and can be represented by a $[K, M, N]$ array of 16-bit numbers where $K = 8$ is the number of filters, $M = 544$ is the usual number of elevation steps for the rebuilt MSPs, and $N = 120$ scans are acquired during each hour (30-second cadence).

15 Ephemeris software (?) was used to calculate the time and elevation corresponding to the transit of Jupiter through the local meridian containing the zenith and terminated by the celestial poles. To start we assumed that instruments were perfectly level and had azimuths pointing directly north in order to obtain a starting point for identifying actual transits. A keogram sub-region centered on the predicted transit was used to fit a two-dimensional generalized Gaussian model

$$\begin{aligned}
 D(x, y) = D_0 \exp \left[- \left| \frac{\bar{x}}{\sqrt{2}\alpha_x} \right|^{\beta_x} - \left| \frac{\bar{y}}{\sqrt{2}\alpha_y} \right|^{\beta_y} \right] \\
 + B_0 \{ 1 + B_x \bar{x} + B_y \bar{y} + B_{xy} \bar{x} \bar{y} \}
 \end{aligned} \tag{29}$$

20 where D_0 and B_0 are signal and background, $\bar{y} = y - y_0$ and $\bar{x} = x - x_0$ are the elevation and time relative to the transit peak x_0, y_0 , $\alpha_{x,y}$ are profile widths, and $\beta_{x,y}$ are scaling parameters. Jupiter transit profiles were initially ~~modelled-modeled~~ with a simpler bivariate Gaussian ($\beta_x = \beta_y = 2$) which could usually achieve model/data differences on the order of 10%. The more general representation in Equation 29 was introduced in an attempt to ensure that model error would not be a limiting factor



Thu Nov 01 20:46:43 2012

c:\Users\bjacke\Dropbox\work\msp\fig\calgary_msp_profile.eps

Figure 6. Gillam MSP observations of Jupiter on November 22, 2011. Shading in central panel corresponds to counts for each scan and step (higher DN are darker, ranging from 0 to 1500 DN), contours indicate best fit 2D Gaussian. Right panel is elevation profile obtained by averaging over time (symbols) and best fit Gaussian (dotted line). Top panel is time profile obtained by averaging over elevation. Dashed lines indicate the predicted transit time (off scale) and elevation for ideal north-south scan.

for analysis at the 1% level. We subsequently found that the coefficients also provided a useful measure for classifying transit quality, and more clearly identified minor azimuthal asymmetry in the optical response.

The polynomial background model is effective for mitigating effects from dawn/dusk gradients and scattered moonlight. This significantly increases the number of transits which could be used for estimating orientation and field-of-view, although relatively few of these additional events are suitable for photometric-radiometric calibration. Figure 7 shows Gillam transit times obtained over three winters several winter field seasons. Sequences of good transits correspond to cloudless nights, gaps and gaps correspond to periods of poor visibility near full Moon.

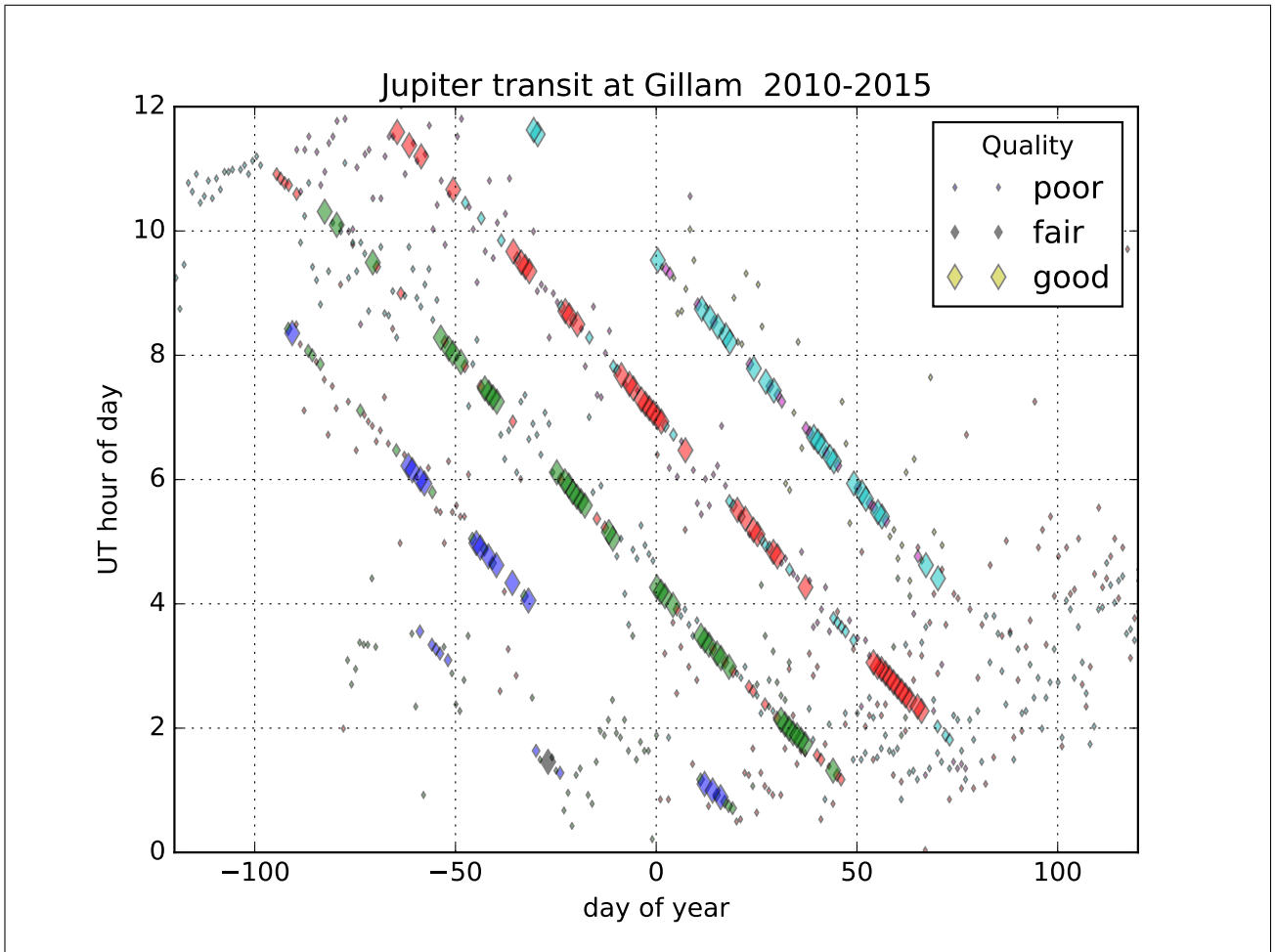


Figure 7. Jupiter transit time (UT) observed at Gillam during 2011-2014 northern hemisphere winters. Each symbol corresponds to a single night.

3.1 Field of view

Stars and distant planets are effectively point sources when viewed with a single pixel detector (PMT) through optics with angular resolution on the order of 1° . Each MSP elevation sweep over an astronomical source will produce a profile that corresponds to the “vertical” optical angular response. Similarly, a time sequence of observations from a fixed elevation should provide a complementary measure of “horizontal” optical beam shape. This is illustrated in Figure 6 with a full two-dimensional (elevation and time) distribution of observed counts along with corresponding elevation and time profiles. Each profile is approximately Gaussian, and the combined two dimensional pattern is fairly well ~~modelled~~ modeled by the bivariate generalized Gaussian in Equation 29. A complete transit profile extends over 10 minutes, during which time viewing conditions may change considerably. In contrast, each elevation sweep over Jupiter lasts for only a few seconds.

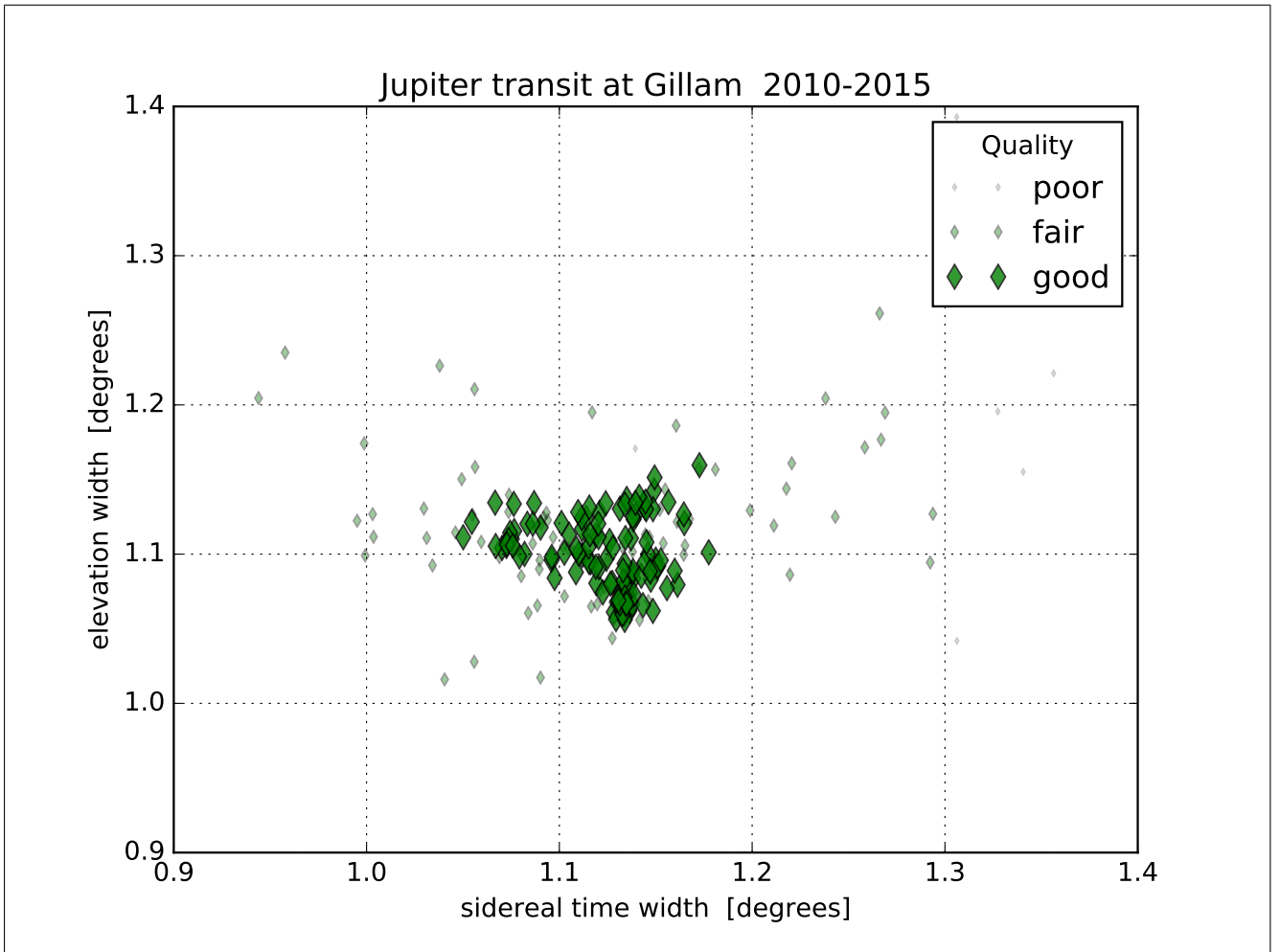


Figure 8. Optical beam width σ determined by fitting a generalized Gaussian to observations of Jupiter by an MSP at Gillam over three winters.

Fitted horizontal (time) and vertical (elevation) beam widths from the Gillam MSP are plotted in Figure 8. There is a cluster of points near $\sigma \sim 1.1^\circ$ that presumably corresponds to the actual beam shape. Other points are generally associated with sub-optimal viewing conditions (eg. clouds or aurora). Seasonal average estimates of horizontal and vertical beam width for Gillam and Fort Smith sites are presented in Table 7. Results are consistent with all instruments having similar horizontal and vertical widths: $\sigma \approx 1.07^\circ$ (FWHM $\sim 3.0^\circ$). Average beam widths have standard deviations less than 0.05° and standard errors less than 0.01° ; typical beam solid angles are approximately 2.30×10^{-3} steradians with uncertainties of a few percent.

The effective solid angle Ω_0 is essential for comparing flux from distant point sources to distributed auroral emissions. For several years of Fort Smith data the average value was 2.07 milliSteradians with standard deviation of 0.12, and standard error of the mean less than 1%.

3.2 Orientation

An ideal MSP would be aligned to produce scans with predetermined azimuth and elevation. For outdoor installations at remote field sites it can be difficult to reduce leveling errors below a few degrees. ~~Further complications may arise as the ground freezes in autumn and thaws in spring.~~ Geographic azimuth may be difficult to precisely determine unless a detailed site survey is available. Alignment with magnetic north can also be challenging unless the site is magnetically clean and there are no geomagnetic disturbances. Over longer periods the magnetic declination may change significantly (see Table 1) due to secular variation in the geomagnetic field.

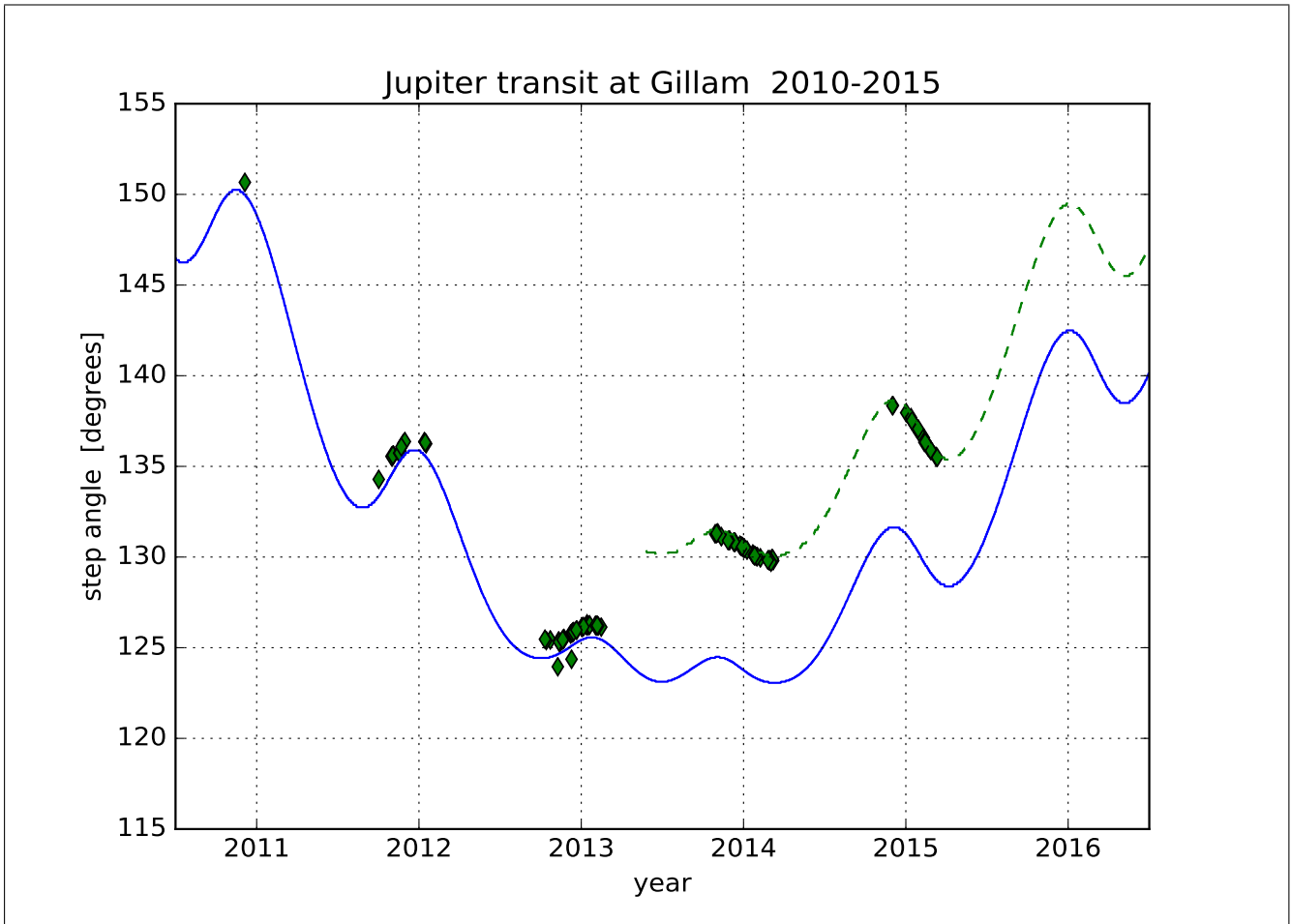


Figure 9. ~~Gillam MSP orientation inferred from observations~~ Nominal stepping mirror elevation of Jupiter as observed by Gillam MSP. Each symbol corresponds to one transit during a single night. ~~Large symbols correspond to~~ “Solid line indicates the actual elevation, while the dashed line is shifted by 7.5 degrees. Instrument alignment was quite good” ~~beam widths with both vertical and horizontal $\sigma \sim 1^\circ$ before summer 2013, after which an unplanned tilt is evident.~~ Small symbols correspond to all other events.

Fortunately, it is possible to accurately determine instrument orientation from transit observations. Starting with site locations obtained using GPS, observed transit times were used to calculate the actual elevation and azimuth of Jupiter for each night. These were interpreted in terms of two device angles. First, azimuth offset was attributed to horizontal orientation of a level instrument. Second, the difference between nominal mirror elevation and actual target elevation was attributed to instrument “tilt” from level.

Results for ~~three seasons at Gillam are shown in Figure 9. Azimuth estimates several seasons of azimuth estimates at Gillam (not shown)~~ are extremely stable over time, with jitter $< 1^\circ$ and no apparent drift. Tilt estimates ~~from the~~ are shown in in Figure 9. The first two seasons are ~~even less variable~~ generally stable, although there appears to be a small jump in early November. Examination of results from the other three sites (not shown) finds a similar feature at Fort Smith (FSMI), a smaller shift at Pinawa (PINA), and no obvious change at Athabasca (ATHA). These results are consistent with “frost heave” occurring in early winter as moisture in the soil freezes. The lack of this effect at ATHA may be due to better foundations for the instrument platform. The large change in tilt at Gillam during summer 2013 occurred around the same time as a maintenance trip. This shift could not have been detected in real-time due to the lack of Jupiter transit data during limited observing hours during summertime operations. Fortunately, once the problem has been identified, it is relatively straightforward to make the necessary corrections to scientific data products.

Table 7. Instrument orientation and beam width from all good transits at Gillam and Fort Smith during each winter. Averages and standard deviations in degrees for azimuth, tilt, beam width, beam height. Solid angle average in milli-steradians and percent standard error.

site	year	N	azimuth	tilt	σ_h	σ_v	Ω
GILL	2011-12	73	6.65 ± 0.16	0.52 ± 0.32	1.04 ± 0.07	1.12 ± 0.06	$2.224 \pm 1.5\%$
GILL	2012-13	67	6.62 ± 0.14	0.54 ± 0.33	1.10 ± 0.05	1.08 ± 0.04	$2.281 \pm 1.0\%$
GILL	2013-14	46	4.81 ± 9.25	6.52 ± 0.77	1.10 ± 0.07	1.09 ± 0.06	$2.301 \pm 1.8\%$
FSMI	2011-12	64	10.35 ± 0.16	0.59 ± 0.29	1.06 ± 0.07	1.11 ± 0.05	$2.257 \pm 1.4\%$
FSMI	2012-13	57	10.00 ± 0.26	0.87 ± 0.19	1.12 ± 0.10	1.07 ± 0.06	$2.282 \pm 2.0\%$
FSMI	2013-14	54	10.50 ± 0.24	0.66 ± 0.22	1.12 ± 0.09	1.06 ± 0.04	$2.274 \pm 1.6\%$

A yearly summary of orientation parameters for ~~each site two sites~~ is presented in Table 7. For cases with 30 or more good transits the standard deviations are less than $1/2^\circ$ and uncertainties in the average (standard errors) are less than ~~0.1° . This~~ 0.1 degrees. This level of accuracy allows data to be accurately mapped into other coordinates (ie. geographic); even minor changes to instrument alignment can be easily identified.

20 3.3 Magnitude variation

The signal intensity during each transit will depend on source brightness, instrument sensitivity, and atmospheric effects. This is complicated for Jupiter, as the apparent visual magnitude varies due to changes in distance from Earth. Figure 10 illustrates the importance of this effect, with predicted variation in apparent brightness following the upper bound of observations. The lower set of events typically correspond to apparent transit profile widths that are significantly different than the best-case

values, and are likely due to non-ideal atmospheric transmission (eg. clouds or ice crystals). There are usually several dozen “good” transits per season; subsequent analysis will focus on these events.

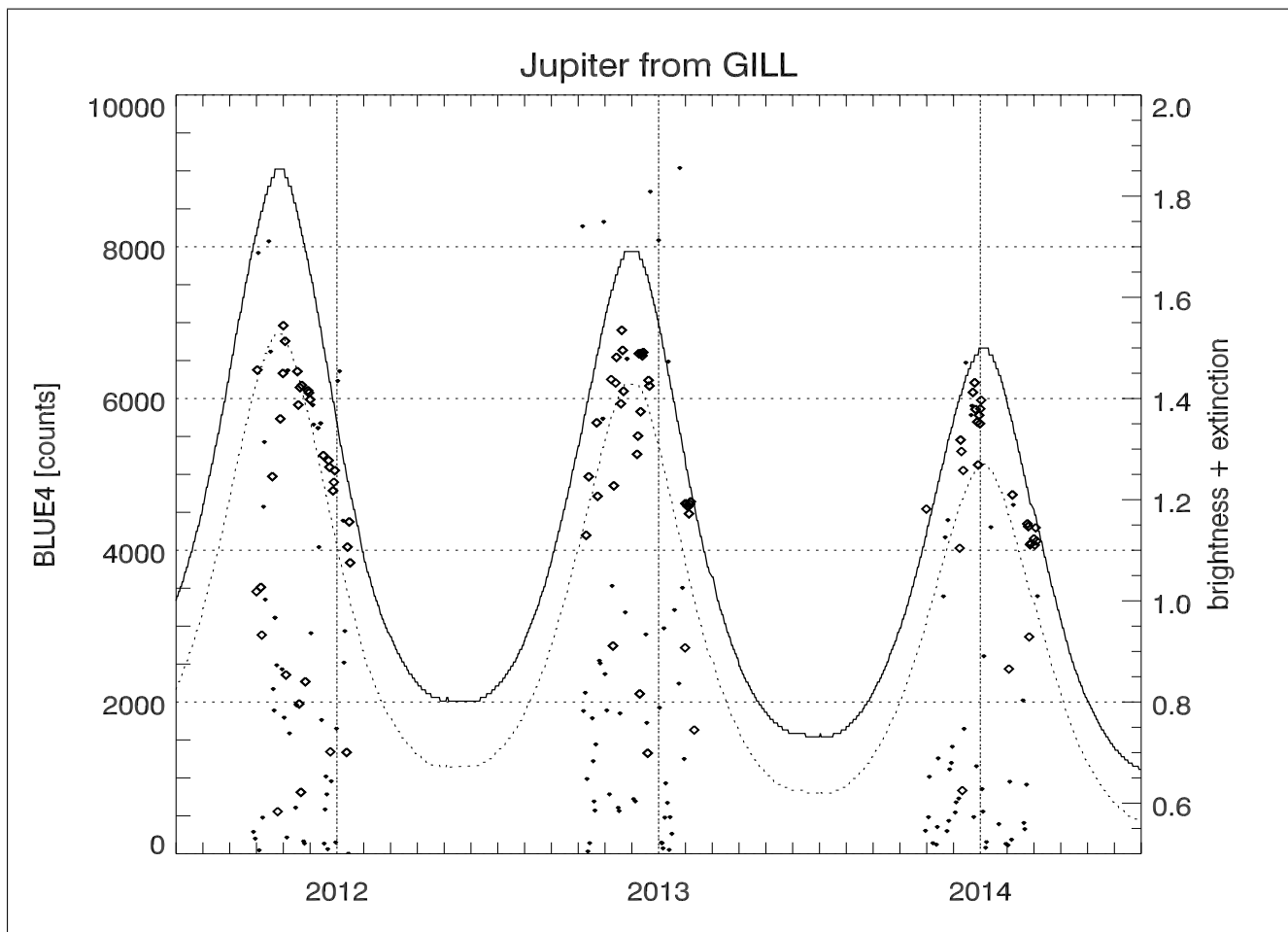


Figure 10. Peak counts from Jupiter at Gillam over three winters. Large symbols are transits with narrow widths, small symbols are noisier profiles. Solid line is variation in apparent visual magnitude of Jupiter, dashed line indicates the change in extinction due to doubling air mass ($\Delta\kappa = 0.15$).

Effects due to variation in source brightness can be removed by normalizing all measured \bar{D} cases to magnitude $m = 0$

$$\mathcal{D}_0 = \bar{D} \times \sqrt[5]{100}^{m_J} \quad (30)$$

- 5 where m_J is the apparent visual magnitude of Jupiter predicted by the ephemeris. The resulting distribution of normalized magnitude at Gillam (not shown) has a fairly narrow peak with a sharp higher cut-off and a long tail of lower values corresponding to non-ideal viewing conditions. The 90th percentile was found to be a simple and robust estimator of peak normalized bright-

ness, while average and standard deviation are used to estimate uncertainty in seasonal averages. Results for Gillam and Fort Smith are presented in Table 8.

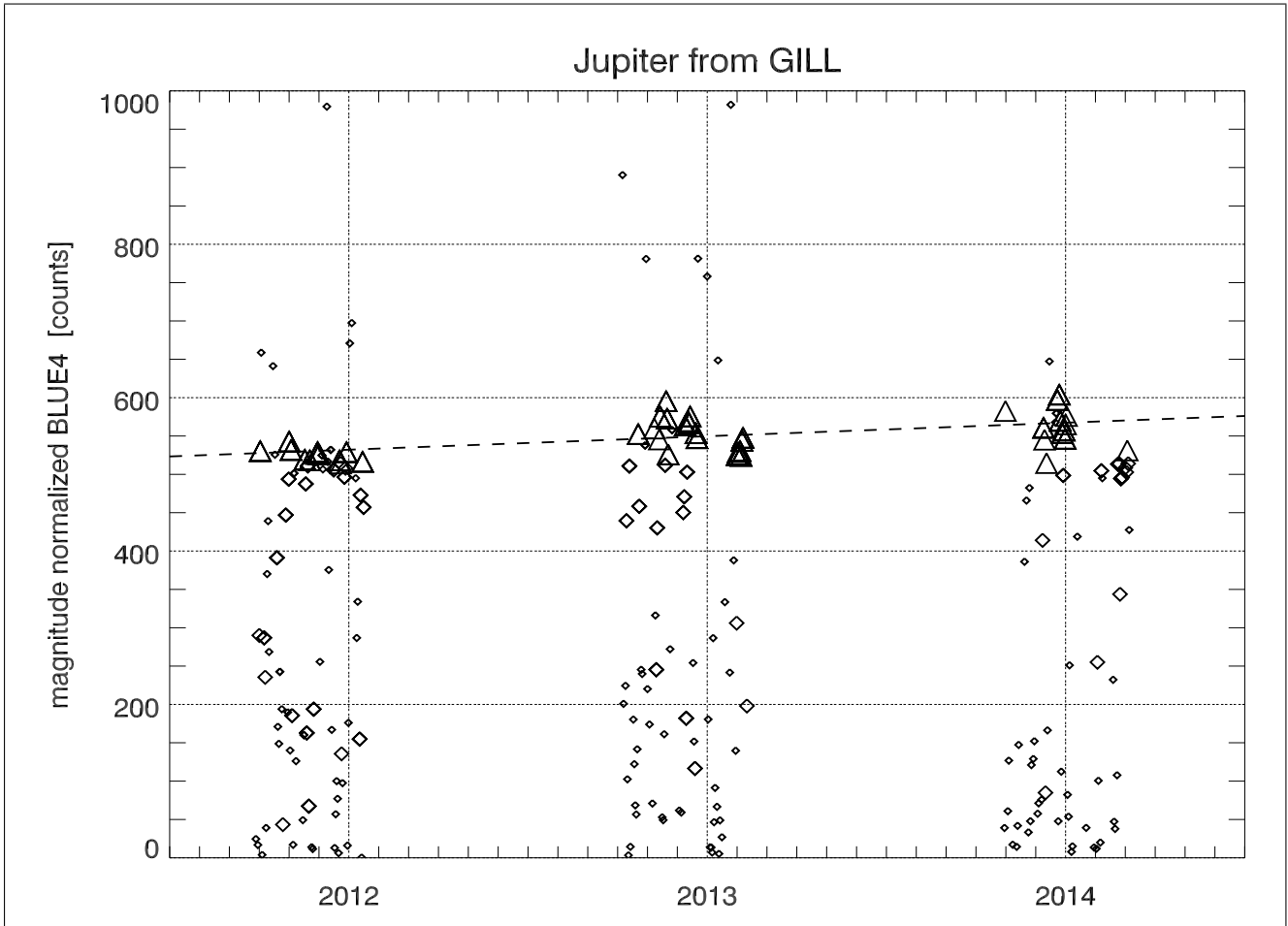


Figure 11. Gillam transit events from Figure 10 normalized to magnitude 0 using Equation 30.

Normalized brightness for all Gillam transits over three years are shown in Figure 11. Linear fits to the data give a slight positive slope of roughly 2% per year, but with statistical uncertainty that includes zero. This is consistent with a stable system response at blue wavelengths, although variations on the order of 5% cannot be excluded.

If the linear trend were significant, this would mean the instrument was becoming slightly more sensitive over time, which seems unlikely. Closer examination of the data found that most of the variation is due to a 5% jump between 2012 and 2013 after which the signal levels remain essentially constant. The jump did not correspond to any system maintenance or modifications. A nearly identical pattern was observed at Fort Smith, further suggesting that the underlying cause was not instrumental.

In fact, this appears to be an example of atmospheric effects as discussed in §1.4.1. The apparent declination of Jupiter increased from $+5^\circ$ in 2011 to roughly $+15^\circ$ in 2013 and 2014. This reduced the transit zenith angle at Gillam from $\zeta = 57^\circ$ to

44°, and effective air mass from $X = 1.84$ to 1.39. For a nominal blue-value-extinction coefficient $\kappa = 0.17$ at blue wavelengths with zenith transmission $K = 85.5\%$ the change in declination corresponds to transmission differences of 74.9% versus 80.4%. Adding this correction to normalized brightness reduces the linear trend to zero, although with considerable uncertainty.

3.4 Spectral ratio

5 Absolute photometric-radiometric calibration with Jupiter is complicated by variability in observed brightness, and absolute spectral sensitivity is similarly challenging. Working with relative spectral response removes changes in source brightness, allowing us to focus on instrumental and atmospheric effects. In order to reduce statistical uncertainty we have normalized all channels to the average of the twin H_β channels ~~and summarized the results~~. Results are summarized in Table 8.

10 Factoring out external brightness variation provides useful information about internal stability of different wavelength channels. Averages for normalized blue channels are essentially constant to within 1% year-to-year. This result provides some reassurance about relative filter stability, but cannot exclude the possibility of any change which might produce identical changes in all channels (eg. high-voltage supply drift, optical defocusing).

15 Red channels exhibit more variability on both short and longer time scales as shown in Figure 12. One notable feature is a clear drop after the first season, followed by two years of relative stability. This might be attributed to some wavelength dependent change in sensitivity such as photocathode aging or filter delamination. However, exactly the same pattern is observed at all four sites, suggesting a cause that is external rather than instrumental.

As noted in §1.4.1, apparent changes in wavelength ratios can also be produced by variations in source declination. Extinction at zenith will have a larger effect on shorter wavelengths, thus increasing the red:blue ratio. This effect becomes larger as zenith angle increases with largest red-to-blue ratios observed near the horizon. From 2012 to 2013 Jupiter's declination increased
20 by roughly 10° and transit zenith angle decreased from 50° to 40° . Assuming that observed changes in wavelength ratio are caused by this effect, a simple log-linearized regression

$$\log I_1/I_2 + \log(2.512) - x(\kappa_1 - \kappa_2) = \log D_1/D_2 \quad (31)$$

gives a slope of $\kappa_{\text{red}} - \kappa_{\text{blue}} \approx 0.38$ which is generally consistent with other results considered in §1.4. Since this estimate is produced by combining a large number of transits obtained during a wide range of atmospheric conditions we do not place too
25 much weight on the precise value. The important result is that spurious trends in wavelength ratios can be ~~modeled~~ modeled well enough to allow detection of real changes on the order of 5%.

3.5 Absolute sensitivity

The System sensitivity defined in Equation 28 provides a measure of the data count rate \mathcal{D} produced by one Rayleigh per nanometer \mathcal{R} of ~~auroral luminosity can be found by using the definition of sensitivity (Equation ??) including atmospheric losses (Equation 20) and the relationship between distributed and point sources (Equation 14)~~ extended luminosity. This can be related to the differential irradiance of an ideal point source using Equation 14. Losses due to atmospheric effects can be

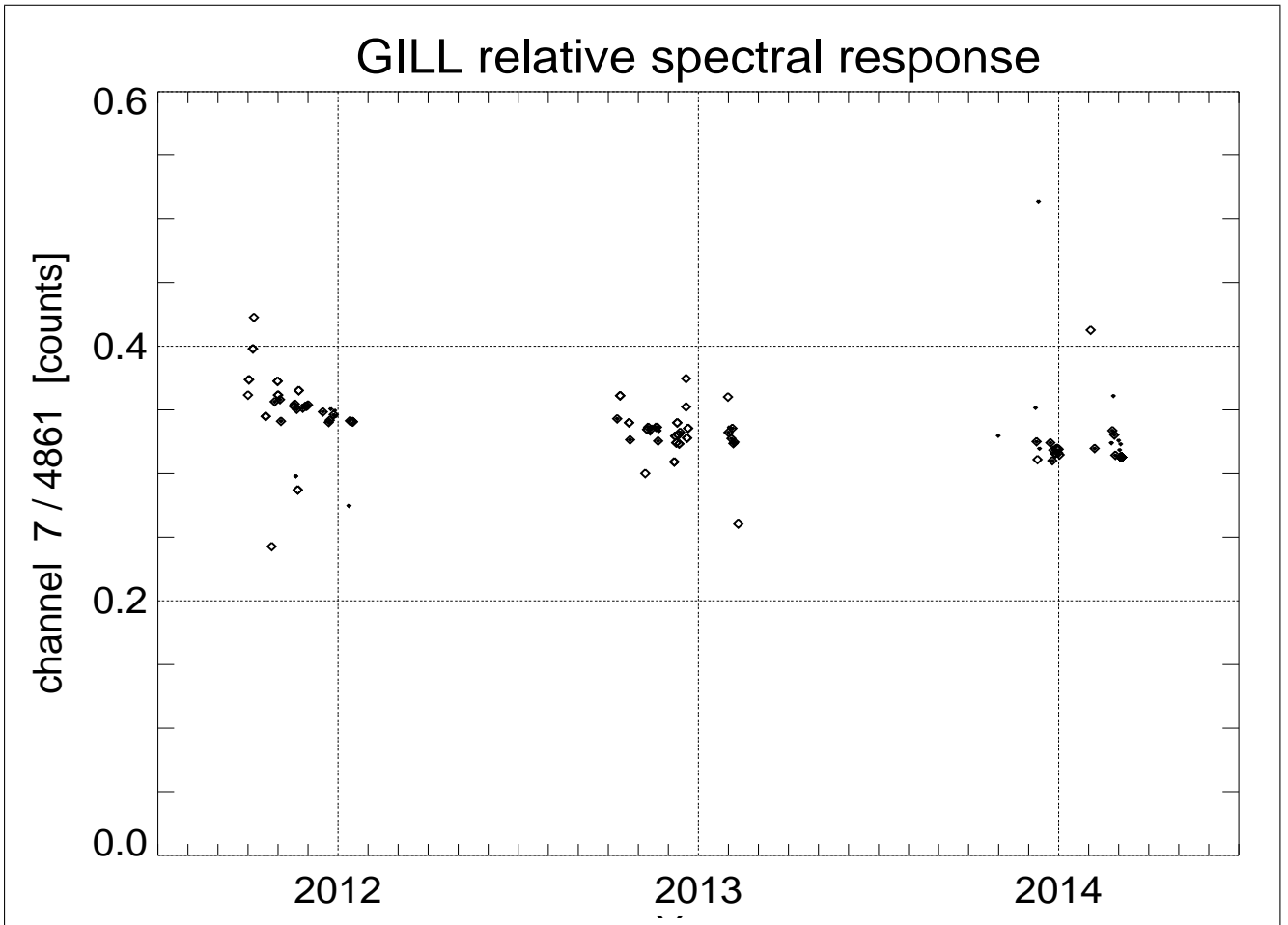


Figure 12. Ratio of 630.0 nm to average of two 486.1 nm channels versus time. Large symbols correspond to good transits and small symbols to noisier events.

[modelled with Equation 20. The combination of these three equations](#)

$$C_{\mathcal{D}/\dot{R}} = 10^{10} \frac{\mathcal{D}}{\dot{S}_\gamma} \frac{\Omega_0}{4\pi} 2.512^{+\kappa X} \quad (32)$$

[to get an expression gives an expression for calibration coefficients](#) in terms of five [physical](#) quantities (see also page 42 of ?).

Three of these terms are easily estimated, while the other two present some challenges.

- 5 The differential number flux \dot{S}_γ of solar photons scattered from Jupiter and arriving at the top of the Earth's atmosphere is only subject to uncertainties in the solar spectrum and Jupiter's albedo, both of which are known to 1% or better. The effective air-mass $X(\zeta(t))$ depends on the apparent zenith angle which can be calculated for any arbitrary time. The effective solid angle Ω is either known *a priori* or can be estimated from transit profiles. ~~From~~; [from](#) §3.1 the uncertainty of an unbiased estimate will be less than 1%, but systematic bias on the order of 5% is also a possibility.

Table 8. Magnitude normalized intensity and self-normalized spectral sensitivity for Gillam and Fort Smith. Column 4 is the 90th percentile of intensity. Column 4 is the source normalized brightness (Equation 30). Remaining columns are channel brightness normalized to average of two 486 nm observations.

site	year	N	90%	\mathcal{D}_0	471	480	486	486	495	558	625	630
GILL	2011-12	73	530.3	425 ± 143	0.914	1.054	0.997	1.003	1.052	0.087	0.415	0.382
GILL	2012-13	67	572.7	474 ± 133	0.927	1.033	1.007	0.993	1.073	0.087	0.399	0.359
GILL	2013-14	46	582.6	487 ± 141	0.914	1.042	0.997	1.003	1.061	0.018	0.376	0.366
FSMI	2011-12	64	844.9	651 ± 224	0.915	1.063	1.000	1.000	1.055	0.071	0.395	0.379
FSMI	2012-13	57	873.2	732 ± 199	0.933	1.043	1.009	0.991	1.066	0.102	0.400	0.341
FSMI	2013-14	54	877.0	715 ± 228	0.907	1.056	1.003	0.997	1.049	0.053	0.387	0.347

The extinction coefficient spectrum $\kappa(\lambda)$ can be highly variable, can have a major effect on received signal levels, and cannot be accurately estimated from the MSP data. In the absence of other information, the best we can do is identify an upper envelope containing the brightest events and assume that they correspond to the minimum possible extinction values. This approach seems to produce intrinsic variability less than 5%, but does not address the issue of systematic bias.

- 5 Each transit could potentially provide a measured value for \mathcal{D} . A simple calculation of Poisson uncertainty for the entire profile would be on the order of 1% assuming good transits with peaks in excess of 2000 counts. This result may be overly optimistic given the complicated nature of many transits. An alternative approach is to examine sequences of transit profiles, focus on clusters of “bright” events in the top quartile or decile, and assume that they provide an overestimate of the intrinsic variability. This approach produces estimated uncertainties ranging from 1-5%.
- 10 Data from a single transit can be scaled by model flux density from Equation [??-18](#) to obtain an empirical estimate of the system calibration coefficient \mathcal{C} . An example is provided in Table 9 for the November 22, 2011 transit at Gillam using the pair of nominally identical 486 nm channels as an example. Fitting a two-dimensional Gaussian model to each channel separately produced very similar peak values: 1501.14 DN and 1501.54 DN. Appropriate model values from Table 3 can be used to predict input photon flux (neglecting atmospheric effects) and estimate a system calibration coefficient relating flux from a
- 15 point source to measured data numbers.

Calculation up to this point has consisted of multiplying several quantities, each with relative uncertainty of a few percent or less. These errors are negligible in comparison to atmospheric variability. The 486.1 nm extinction factor at zenith could vary between 0.73–0.84 for fair to good visibility, and 0.64–0.78 at $\zeta = 45^\circ$. Lower elevations and worse viewing conditions will further attenuate incoming flux. Neglecting extinction will provide a lower bound for empirical sensitivity, as reduced flux

20 requires higher sensitivity in order to produce the same observations.

Including more events should provide some combination of additional information and increased variability. We attempt to focus on a sub-set of “high-quality” transits that presumably correspond to good atmospheric viewing conditions. Events are first classified according to beam widths (§3.1). Most points cluster near a common linear trend, but there are also quite a few low-brightness outliers. A robust (least absolute deviation) linear model provides a plausible fit that is insensitive to

Table 9. Calibration coefficient $\mathcal{C}_{\mathcal{P}/\mathcal{D}}$ estimated at Gillam using a single transit on November 11 2011. Atmospheric effects are neglected.

486.1	[nm]	channel wavelength
1501	[DN]	peak data number
5.191×10^{17}	[photon]/[m ² · s · nm]	solar photon flux at 1 AU
5.328×10^{-10}		geometric factor $A(t)$
0.455		jupiter albedo
1.061×10^9	[photon]/[m ² · s · nm]	jupiter photon flux at Earth
7.067×10^5	[photon]/[m ² · s · nm · \mathcal{D}]	calibration coefficient $\mathcal{C}_{\mathcal{P}/\mathcal{D}}$
0.799		extinction at $\zeta = 45.6^\circ$

outliers. Points within a generous range around the robust fit are classified as high-quality and used for subsequent analysis, including standard least squares estimates of intercept and slope $\mathcal{C}_{\mathcal{D}/\mathcal{P}}$. Figure 13 shows classification and fitting results for the combined blue channel data. This automated process produces reasonable results for all the data considered in this study.

[Channel calibration coefficients for Gilliam and Fort Smith are presented in Table 10.](#) More sophisticated algorithms for further

5 studies could explicitly include the asymmetric nature of extinction ie. hard upper bound on theoretical maximum.

Table 10. Sensitivity for each channel in Data Numbers (counts) per Rayleigh per nanometer $\mathcal{C}_{\mathcal{D}/\mathcal{R}}$.

	year	N	471	480	486	486	495	558	623	630
gill	2011	59	0.2478	0.1816	0.2507	0.2427	0.2002	1.6296	1.0857	0.9721
gill	2012	60	0.2114	0.1603	0.1698	0.1702	0.1718	****	0.8244	0.8764
gill	2013	39	0.1434	0.1280	0.1169	0.1174	0.1365	1.3462	0.5802	0.5037
fsmi	2011	51	0.0734	0.0707	0.0615	0.0611	0.0704	1.5203	0.3267	0.3525
fsmi	2012	47	0.1239	0.1182	0.1096	0.1113	0.1292	3.6000	0.6915	0.6828
fsmi	2013	52	0.1316	0.1222	0.1164	0.1164	0.1307	3.3278	0.5578	0.3469

4 Discussion

When auroral instruments operate unattended for long periods of time at remote locations, frequent comprehensive on-site calibration may not be feasible. If celestial objects can be identified in standard data streams then these may serve as the basis for alternative independent calibration procedures.

10 ~~There is a long history of using astronomical sources to determine the alignment of auroral instruments (?). Absolute calibration using stellar spectra appears to be a more recent development ??????. Details discussions of these topics are not always found in the primary scientific literature, but must often be extracted from conference proceedings, technical reports, and theses. Fortunately, these resources are more easily discovered with modern search engines.~~

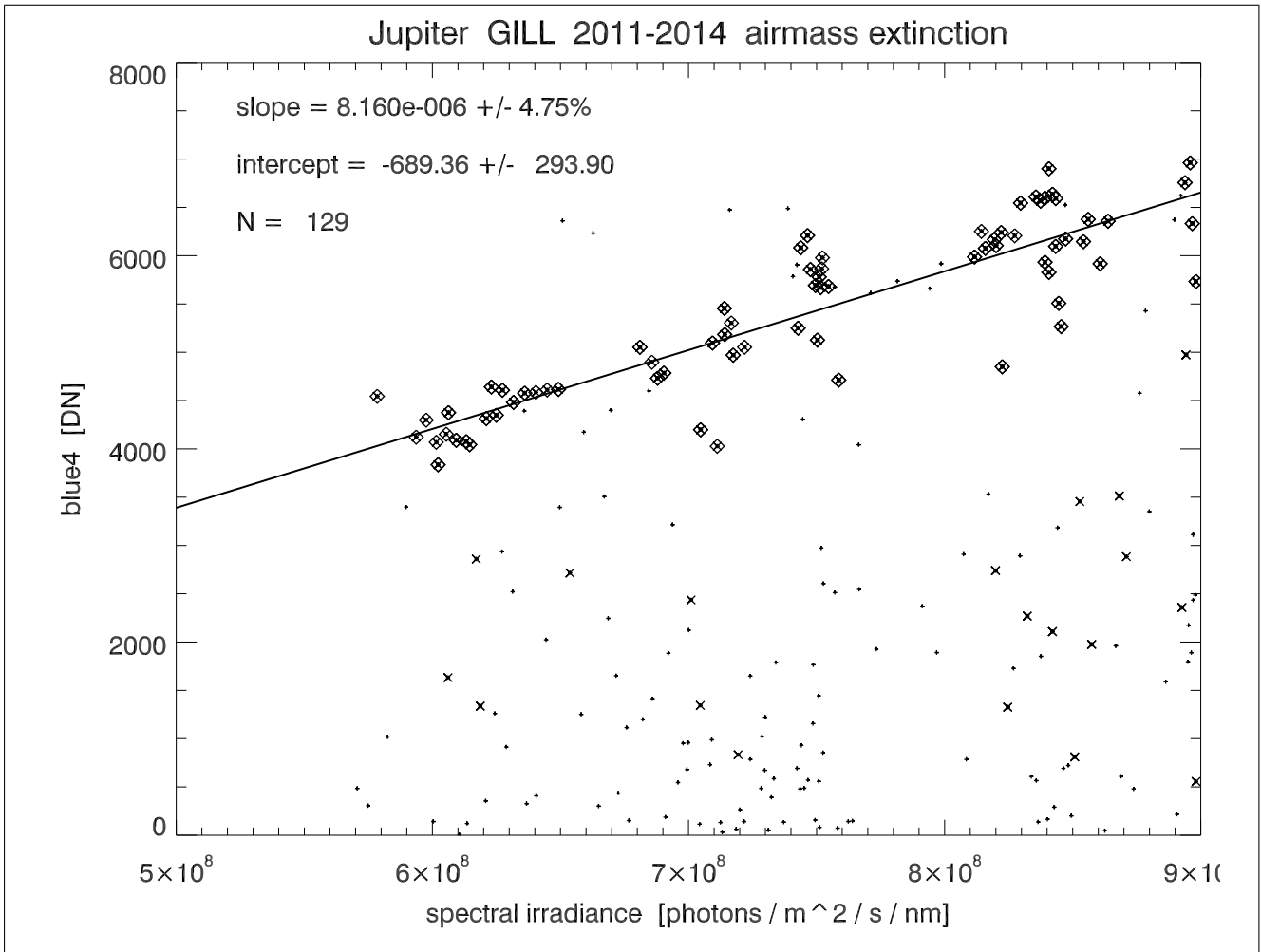


Figure 13. Total counts in four blue channels (excluding 470.9 nm) as a function of predicted photon flux density. Small “+” indicate all cases, medium “x” for good beam widths, large squares for nearness to robust fit line. Flux model includes solar spectrum, illumination geometry, Jupiter albedo, and terrestrial atmospheric extinction as in Table 3.

Stars are essentially point sources when viewed using auroral instruments with angular resolution on the order of 1° . They are stationary in celestial coordinates, and follow predictable paths as the Earth moves during each day and over the course of a year. Absolute flux spectra are increasingly available, although more generally for faint stars that cannot be reliably detected by most auroral devices. Even the brightest stars are only comparable to low-intensity aurora with correspondingly high statistical uncertainty. Light from extra-terrestrial sources must also travel through the Earth’s atmosphere before arriving at a detector. The resulting wavelength-dependent reduction in photon flux depends critically on atmospheric properties that may not be well known. Of course, auroral light is also subject to the same atmospheric effects.

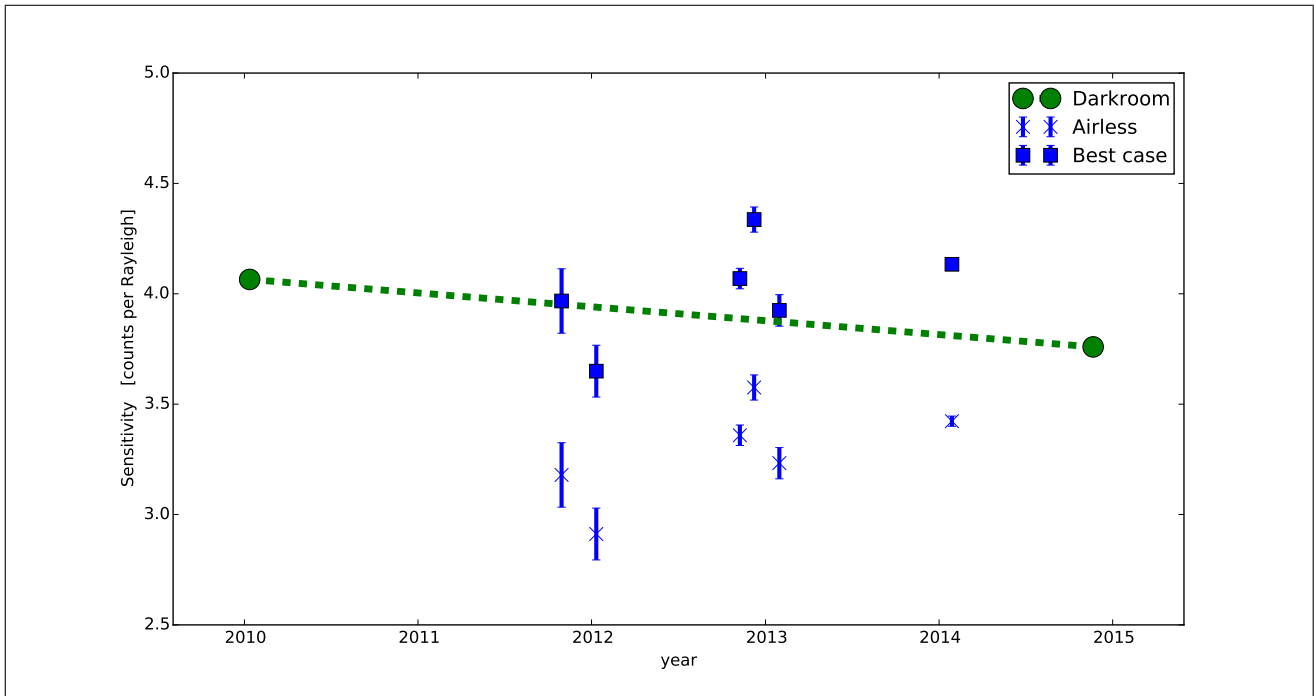


Figure 14. Sensitivity for the FSMI MSP 486.1 nm channels. Green circles are values obtained during darkroom calibration in 2010 and 2014, nominal linear trend of -2%/year indicated by dashed line. Blue symbols are values obtained by averaging three best values over 10-day intervals and standard deviation indicated with error bars, x's are without any atmospheric correction, squares are with “clear sky” model.

Jupiter’s peak radiance-intensity is greater than the brightest star, but less than the moonmoon, so there is no risk of saturating most auroral detectors. It is effectively point-like, has a predictable trajectory, and absolute spectral flux can be calculated from existing albedo and solar irradiance measurements. Unlike stars, planets are not fixed in celestial coordinates, meaning that transit altitude is not constant. This minor complication actually provides an opportunity to study the effects of changing zenith angle on atmospheric extinction.

4.1 Atmospheric effects

Atmospheric transmission is likely to be the largest source of uncertainty for high SNR applications. Reducing this uncertainty will require estimation of extinction coefficients that are appropriate for each transit. Our preliminary attempts to determine these parameters using multi-spectral MSP data were not successful, but this problem may yield to more sophisticated analysis. In principle, extinction coefficients can be found simply by measuring the apparent magnitude of a single star at a given wavelength over a range of different zenith angles. Improved precision can be achieved by combining data from multiple stars. Many auroral observatories include all-sky camera systems which can image dozens or hundreds of stars. However, the optical response (“flat field”) of these systems is also a strong function of axial angle, which for an ASI is usually directed towards the

zenith. Accurate flat-fields will be essential for accurate extinction estimates. Recent work by ??? might be adapted for auroral applications.

It is tempting to avoid the ~~complexity~~ complexity of atmospheric variation by using only a small number of “good” days to determine calibration parameters. One obvious limitation of this approach is that it cannot reliably detect short term changes in instrument response. More importantly, all auroral observations are subject to exactly the same atmospheric issues. ~~An are A~~ constant emission feature moving from the horizon to zenith will ~~become brighter, not because of any change in precipitation,~~ but appear brighter even after accounting for viewing geometry (i.e. Van Rhijn correction) simply due to the reduction in total airmass between auroral altitudes and a ground-based observer. Atmospheric effects may be negligible when looking directly upward through clear skies, but critically important at low elevations and non-ideal viewing conditions. These effects would be even more pronounced at shorter wavelengths (eg. 427.8 nm and 391.4 nm) often used in auroral studies.

4.2 Retrospective Calibration

Some auroral instruments only acquire data during short-term “campaigns”, but many are operated in support of longer term science objectives. Not all devices are fully calibrated before being deployed and few are calibrated on a regular basis. Even when the resulting data overlap in space and time, quantitative comparison may not be possible. Astronomical observations of bright sources such as Jupiter can provide a basis for retrospective cross-calibration of historical data sets.

The original CANOPUS ~~meridan~~ meridian scanning photometer array (MPA) is a good example. Digital “low resolution” binned data are available starting in early 1988 and continuing until spring 2005. Some higher resolution data are available for the transition period from 2005-2010, after which all refurbished instruments were operating in the same high-resolution mode. The 16 years of low-res data alone extend well beyond one solar cycle and could span more than two if merged with newer data.

However, certain kinds of quantitative analysis are limited by the lack of ~~photometric~~ radiometric calibration. Some key parameters (eg. filter band-width and channel sensitivity) were determined for each system, but the supporting documentation is very limited. Mechanical and electrical subsystems were regularly maintained and repaired, but there was no corresponding ~~calibration~~ re-calibration schedule. Some terminal calibration procedures were carried out during the 2005-2010 transition, but by this point the instruments were often not functioning reliably. In order to confidently identify long-term geophysical trends in these data it is essential to have some sense of how instrument performance changed over the same time-scales.

A preliminary survey of the CANOPUS MPA data archive has confirmed the feasibility of astronomical calibration and also identified some significant challenges. First, only the brightest few stars are visible even with optimal viewing conditions. Jupiter can be clearly identified, but at count rates much lower than obtained by the newer systems, and consequently with much greater uncertainty. Elevation steps are combined into 17 latitude bins which effectively removes the ability to determine instrument tilt. More generally, it eliminates virtually all information about the optical beam-shape in that direction, including that required to confidently estimate the effective solid angle Ω_0 . Finally, the decreased scan cadence of one-per-minute will slightly reduce the accuracy of azimuth estimates. Despite these limitations it should still be possible to estimate absolute

sensitivity using Jupiter transits during extended intervals at both ends of the project: 1989-1993 and 1999-2005. Other bright stars or planets might be used to fill in the intervening period.

5 Conclusions

In this study we have demonstrated the feasibility of using Jupiter to calibrate a network of auroral meridian scanning photometers. ~~This~~ During times when Jupiter is visible in the night sky it can be easily distinguished from other astronomical sources. Statistical uncertainty may be a limiting factor even for bright stars, so the increased signal from Jupiter is highly advantageous. Addition precision can be achieved by combining results from multiple days with good viewing conditions.

For geometric calibration, this approach provides an estimate of instrument orientation for each transit with even marginal viewing conditions. ~~Abrupt changes~~ Changes of less than 1° between successive transits can be easily identified. ~~If orientation is constant then it~~ Absolute orientation can be determined to at least $1/10^\circ$, which exceeds most application requirements. Angular optical response (beam-shape) can be ~~obtained from a sequence of meridian scans obtained during the transit of a point source.~~ Statistical uncertainty may be a limiting factor even for bright stars, so the increased SNR from Jupiter is highly advantageous. estimated to roughly 1% precision by combining several dozen transits.

Relative spectral calibrations (ratios of different channels) can also be obtained with precisions on the order of 1% during a single field season. Absolute radiometric calibration for individual channels is significantly less precise. This is due primarily to the difficulty of obtaining and identifying perfectly “clean” transits. Even results from apparently ideal transits can differ by 5-20%, likely due to uncertainties in the true atmospheric extinction parameters.

The merits of Jupiter as a calibration source also apply to other types of auroral instruments. Utility of stellar calibration for all-sky imagers has been demonstrated (???) and these methods would be even more effective with a brighter source. Given the complexities of absolute calibration, it might be helpful if observations were presented in some standard format, eg. data numbers normalized to source magnitude \mathcal{D}_0 as defined in Equation 30. This, along with estimates of solid angle Ω_0 and bandwidth $\Delta\lambda$, would greatly facilitate the inter-comparison of different data products, which would be beneficial for both instrument operators and end-users of scientific data products.

In principle, astronomical calibration could be extracted from almost any auroral data set. In practice, this process is typically applied on a case-by-case basis and requires a considerable amount of human intervention and instrument specific knowledge. The essential next step is to develop automated software tools which can be applied more broadly. This will significantly increase the utility of optical auroral observations for quantitative scientific analysis.

Acknowledgements. Funding for ~~refurbishing the MSPs and operating them~~ MSP refurbishment and ongoing operation was provided by the Canadian Space Agency under ~~contracts #??~~ Go Canada initiative contract 13SUGOHSTO for the H STORM project. Field operations support is provided by SED systems and Athabasca University.